

Location, location: optimal placement of new electricity production in the nordic energy system amidst large-scale electrification

Downloaded from: https://research.chalmers.se, 2025-10-23 06:50 UTC

Citation for the original published paper (version of record):

Bertilsson, J., Göransson, L., Johnsson, F. (2026). Location, location, location: optimal placement of new electricity production in the nordic

energy system amidst large-scale electrification. Renewable Energy Focus, 56. http://dx.doi.org/10.1016/j.ref.2025.100765

N.B. When citing this work, cite the original published paper.

research.chalmers.se offers the possibility of retrieving research publications produced at Chalmers University of Technology. It covers all kind of research output: articles, dissertations, conference papers, reports etc. since 2004. research.chalmers.se is administrated and maintained by Chalmers Library

ELSEVIER

Contents lists available at ScienceDirect

Renewable Energy Focus

journal homepage: www.elsevier.com/locate/ref



Location, location: optimal placement of new electricity production in the nordic energy system amidst large-scale electrification

Joel Bertilsson*, Lisa Göransson, Filip Johnsson

Department of Space, Earth and Environment, Energy Technology, Chalmers University of Technology, Gothenburg, Sweden

ARTICLE INFO

Keywords: Energy systems modeling location of renewable power solar PV wind power power transmission

ABSTRACT

Renewable electricity generation is expected to play a pivotal role in the global shift toward electrification. However, the inherent variability of renewable energy sources, in addition to factors such as local weather patterns and grid limitations, poses a significant challenge in terms of determining the optimal size and placement of distributed generation units. This study tackles this issue by applying a novel, high-resolution energy systems model that is tailored to the Nordic region. The model is designed to capture with high accuracy local nuances in relation to grid infrastructure, weather patterns, and demand profiles. The model minimizes the total system costs, accounting for both investment and operational expenditures, through the optimal integration of variable renewable energy sources and dispatchable generation units. The findings indicate that the siting of renewable generation is primarily influenced by a combination of a high number of full-load hours and proximity to the electricity demand, with the latter becoming increasingly important under high-demand conditions. Among renewable technologies, solar photovoltaic systems exhibit the strongest correlation with demand center proximity, whereas offshore wind is mainly constrained by a high potential annual production capacity. In addition, assumptions regarding the availability of electricity grid capacity are shown to have a significant impact on the results, with up to 26% of production being relocated when 100 % thermal grid capacity is available, as compared to when 30% of grid capacity is reserved for contingency events.

1. Introduction

Global electricity demand is projected to nearly double by Year 2050 compared to the Year 2023 levels, according to estimates from the International Energy Agency [1]. A significant portion of this increased demand is expected to be met by variable renewable energy (VRE) sources, such as wind and solar photovoltaic (PV) systems. However, their non-dispatchable nature makes the optimal siting and sizing of these technologies – considering local weather patterns, transmission grid limitations, and proximity to demand – a challenging problem with potentially substantial impacts on system costs.

The optimal localization of distributed generation has been researched from both the energy system modeling perspective, which commonly aims at minimizing the total system costs, and the power grid perspective, which focuses on the physical constraints within the distribution grid, such as power losses, voltage control, reliability and stability [2]. From the power grid perspective, several methods have been developed, including Analytical methods (e.g., the 2/3-rule [3] and the Index Method [4]), Heuristic methods (e.g., the Genetic Algorithm

[5], Tabu search [6], Particle Swarm Optimization [7], Ant Colony Search Algorithm [8]), and Numerical methods (e.g., Gradient Search [9], Mixed non-linear programming [10], Dynamic programming [11]). Comprehensive reviews on the subject have been presented by Prakash and Khathod [12], Georgilakis and Hatziargyriou [2], Shebaz and Patel [13] and Pesaran et al. [14].

From an energy system modeling perspective, the question of optimal localization of wind and solar power has been explored from a more spatially aggregated perspective, with less emphasis on the physical grid constraints and properties. Such studies have frequently focused on assessing the potential benefits of large-scale renewable energy coordination and enhanced grid interconnectivity. Brown et al. [15] investigated the optimal siting of generation using VRE sources from a pan-European perspective, focusing on sector coupling and the impact of the inter-continental transmission grid. They modeled each country as a node and conclude that interconnecting several countries helps to smooth variations, especially those arising from wind power generation, across the continent, although the largest benefit in relation to total system cost is derived from sector coupling flexibility.

^{*} Corresponding author at: Chalmers Tekniska Högskola, Institutionen för rymd-, geo- och miljövetenskap, 412 96 Göteborg, Sweden *E-mail address*: joel.bertilsson@chalmers.se (J. Bertilsson).

Using a similar modeling approach, Schlachtberger et al. [16] investigated the optimal siting of wind and solar power units in Europe, comparing two strategies for balancing variability: local storage and transmission grid expansion. The study, which relied on a highly aggregated representation of the transmission grid, concludes that wind power variations can be effectively smoothed through grid expansion, while PV fluctuations are most-efficiently managed with short-term storage solutions, such as batteries.

Copp et al. [17] investigated the optimal sizing and placement of distributed energy resources in a system powered entirely by wind and solar PV, using New Mexico, USA as a case study. The study highlights the importance of regional trade in reducing curtailment and emphasizes that combining wind and PV can significantly lower system costs, as compared to relying on a single technology.

Other studies have examined similar interactions between different VRE sources and their optimal placement, focusing on regions such as the Middle East [18,19], South America [20] and North America [21], , and various countries in Europe [22–24].

These studies typically employ capacity expansion models for scenarios that feature high shares of wind and solar PV in the energy mix but that operate at relatively low spatial resolution. This limitation has two primary effects on the modeling outcomes: (i) it dilutes the identification of optimal sites for generation using VREs by averaging the capacity factors over large areas; and (ii) it reduces the visibility of transmission bottlenecks in the electricity grid [25]. The impacts of these effects on the modeling results have been investigated by Frysztacki et al. [23], who have presented a novel methodology that separately assesses the influence of spatial resolution on energy modeling with a high share of renewable power production. Their findings indicate that spatial resolution significantly affects the results, with greater geographic detail potentially increasing total system costs by up to 23%, primarily due to transmission bottlenecks that become apparent at higher resolutions. Their study also highlights substantial changes in the shares of onshore and offshore wind power in response to spatial resolution. Higher resolution enables the identification of more-favorable sites for onshore wind, resulting in a greater share of onshore wind power capacity as fewer nodes are aggregated. The study emphasizes the critical importance of having high spatial resolution for making reliable technology choices, particularly in scenarios where grid expansion is constrained or not permitted.

Several studies have examined the impacts of geographic resolution in energy system modeling [25–31]. Krishnan and Cole [27] have analyzed the value of high spatial resolution in capacity expansion models using the ReEDS model. By comparing three levels of spatial resolution, they demonstrate that the competitiveness of renewable resources for electricity production is significantly influenced by the chosen level of resolution. Their findings indicate that PV investments are particularly sensitive to the level of spatial aggregation, with higher aggregation levels leading to reduced PV deployment in favor of wind resources.

Kiala and Mahfouz [28] and Frysztacki et al. [26] focused on how geographic clustering should be performed to preserve local characteristics and grid bottlenecks. Both studies emphasized the importance of avoiding clustering based on political entities, advocating instead for methods that consider transmission grid constraints. Frysztacki et al. [24] concluded that hierarchical clustering methods yield moreaccurate results than commonly used *k*-means clustering, as they better preserve the grid topology limitations.

Findings from the literature underscore the importance of the high spatial resolution adopted in the present study. Notably, Fürsch et al. [32] have demonstrated the value of detailed spatial modeling by analyzing grid expansion in Europe using an iterative approach between an investment and dispatch optimization model and a load flow model, covering 224 nodes across the continent. They show that large-scale grid expansion that allows for optimal utilization of renewable energy sites is almost always beneficial from a low-cost perspective. It is only in certain

areas of Central Europe, located far from large heavy power consumption centers, that the cost of grid expansion is not motivated from the system perspective.

Using a different modeling framework, Tröndle et al. [33] have compared the total system costs on different geographic balancing scales: continental, national, and regional. Their model includes the electricity supply and demand across 497 European regions, based on administrative boundaries. Similar to Fürsch et al. [32], Tröndle et al. conclude that balancing wind and solar variations is most efficient at the continental scale. Their results also show that restricting balancing to a regional or national level is a possibility if grid expansion is constrained, although it can incur a cost penalty of up to 20%.

The optimal placement of onshore wind has been analyzed by Obermüller [34], who compared wind energy valuation under nodal and zonal market structures. Using the PyPSA modeling framework for Germany, represented by a 575-node model, the study demonstrates that zonal pricing – where large areas are aggregated – can lead to suboptimal wind investments, increasing grid congestion and lowering the overall system value of wind energy. The study concludes that wind energy subsidy schemes that are directing new capacity towards system-optimal locations could help to mitigate inefficient investment signals caused by zonal pricing.

The high spatial resolution applied in these studies enables the investigation of local parameters – such as weather conditions, demand characteristics, and grid connections – that influence the placement of distributed electricity generation sources. However, previous studies have typically relied on administrative borders, which fail to capture real grid bottlenecks because they have a restricted time resolution, lower geographic scope with respect to investment and dispatch modeling, and provide only limited representations of VRE-based electricity production.

This work is novel in that it develops and applies an energy systems model that optimizes the localization and sizing of distributed generation, including both VRE and dispatchable production units, with high geographic resolution, accounting for both investment and dispatch costs. It also incorporates a detailed representation of local conditions for wind and solar power within a grid representation in the model, which is validated using a full AC power flow model. In addition, the applied model integrates multiple energy carriers (electricity, heat, and hydrogen) alongside a comprehensive representation of hydropower, which is the dominant electricity production source in the modeled region. Within this modeling framework, this study aims to answer the following questions:

- What are the key factors that influence the cost-optimal placement of new electricity production in a high-resolution spatial energy systems model of the Nordic energy system concomitant with largescale electrification?
- How do different levels of increased electricity demand and power grid availability impact this placement?

2. Method

2.1. General model formulation

This work presents a newly developed linear optimization model, the EHUB Nordic model, which has been designed to minimize investment, maintenance and operational costs while adhering to economic and technical constraints. The model encompasses 342 nodes across Norway, Sweden, and Finland, and the DK2 price area in Denmark, all of which share the same synchronous grid. The 342 nodes correspond to existing substations in the transmission grid, based on ENTSO-E data, and are geographically defined using a Voronoi cell distribution. The model is exogenously provided with specific demands for electricity, heat, hydrogen, and transportation for each node. In addition, it considers potential wind and solar power generation based on the available

land and meteorologic conditions in each individual node.

An overview of the EHUB Nordic model is provided in Fig. 1. The optimization process minimizes investment and dispatch costs over an entire year, with a time resolution of 3 hours, using 2019 as the reference weather year. The model applies a greenfield approach, assuming no pre-existing production technologies or storage systems, with the only exceptions being the inclusion of existing hydropower and nuclear capacity within the modeled region. No emissions of fossil $\rm CO_2$ are permitted and all investment decisions are driven by the projected energy demands and costs for Year 2040.

The model's objective function seeks to minimize the total system cost over the entire modeled year, incorporating both operational costs and annualized investment costs, and can be written as:

MIN : cto

$$= \sum_{n} \sum_{i} \left(\left(C_{i}^{inv} + C_{i}^{OM_{fix}} \right) * s_{i,n} + \sum_{t} \left(C_{i}^{run} * (p_{i,t,n} + q_{i,t,n}) + c_{i,t,n}^{start} + c_{i,t,n}^{part_{load}} \right) \right) + \sum_{r} \sum_{n} \sum_{t} \left(C_{t,r}^{imp} * w_{t,n,r}^{imp} \right)$$

$$(1)$$

where c^{tot} is the total system cost that is to be minimized, C_i^{tnv} represents the annualized investment costs, and $C_i^{OM_{fix}}$ is the fixed operational costs for all technologies (i). The sum of these factors is multiplied by the new installed capacity $(s_{i,n})$ of each technology in each node (n). The running cost (C_i^{run}) , including both fuel costs and the variable operation cost, is multiplied by the sum of the produced electricity $(p_{i,t,n})$ and heat $(q_{i,t,n})$ at each timestep (t) for each technology and node. The start-up cost $(c_{i,t,n}^{start})$ is the cost associated with starting additional thermal power plants, while the part-load cost $(c_{i,t,n}^{part_{load}})$ is calculated based on the difference between the capacity of the power plant currently in operation and the actual production level for each timestep for thermal plants. These two costs are included as variables in the model, which is further

described in Section 2.1.5. The cost of imported electricity $(C_{t,r}^{imp})$ through DC connections to neighboring regions (r) outside the Nordic countries is multiplied by the import level $(w_{t,n,r}^{imp})$ for each timestep and node. The import level is permitted to take a negative value to account for electricity exports.

At all timesteps, the produced electricity, heat and hydrogen must match the demand for each node. For electricity, this can be written as a nodal balance:

$$\begin{split} D_{t,n}^{el} + b_{t,n}^{ch} + PEV_{t,n}^{ch} + HEV_{t,n}^{ch} + \sum_{i \in I_{PH}} \frac{q_{i,t,n}}{\eta_i} + D_n^{ind,const} + h2_{t,n}^{el} + eaf_{t,n}^{el} \\ + \sum_{m} f_{t,n,m}^{trans} + I_{t,n}^{trans,loss} &\leq \sum_{i \in I_{el}} p_{i,t,n} + b_{t,n}^{dch} + \sum_{r} w_{t,n,r} \forall t, n \end{split} \tag{2}$$

The left-hand side of this equation is the sum of the electricity demand at each timestep and node, and includes the: historic electricity demand $(D_{t,n}^{el})$; charging of stationary batteries $(b_{t,n}^{ch})$; charging of personal electric vehicles $(PEV_{t,n}^{ch})$ and heavy electric vehicles $(HEV_{t,n}^{ch})$; and the electricity for power-to-heat, calculated as the heat produced divided by the technology efficiency, $(\frac{q_{it}}{n_i})$. In addition, three types of industrial electricity loads, chosen to represent different levels of demand flexibility, are included: electricity demand at a constant level from new industrial establishments ($D_n^{ind,const}$); electricity fed to electrolyzers for hydrogen production $(h2_{t\,n}^{el})$; and electricity fed to electric arc furnaces in the steel industry $(eaf_{t,n}^{el})$ (further details in Section 2.3.6). Electricity can be transferred $(f_{t,n,m}^{trans})$ from node (n) to a neighboring node (m) through the transmission grid, and this is associated with a loss $(l_{t,n}^{trans,loss})$ that is assumed to occur in the sending node. The transferred power is allowed to take negative values to allow for the import of power to a node, while the loss is based on the absolute quantity of transferred electricity and is, thus, always positive. The sum of the electricity demands is, for each timestep and node, less than or equal to the sum of the produced

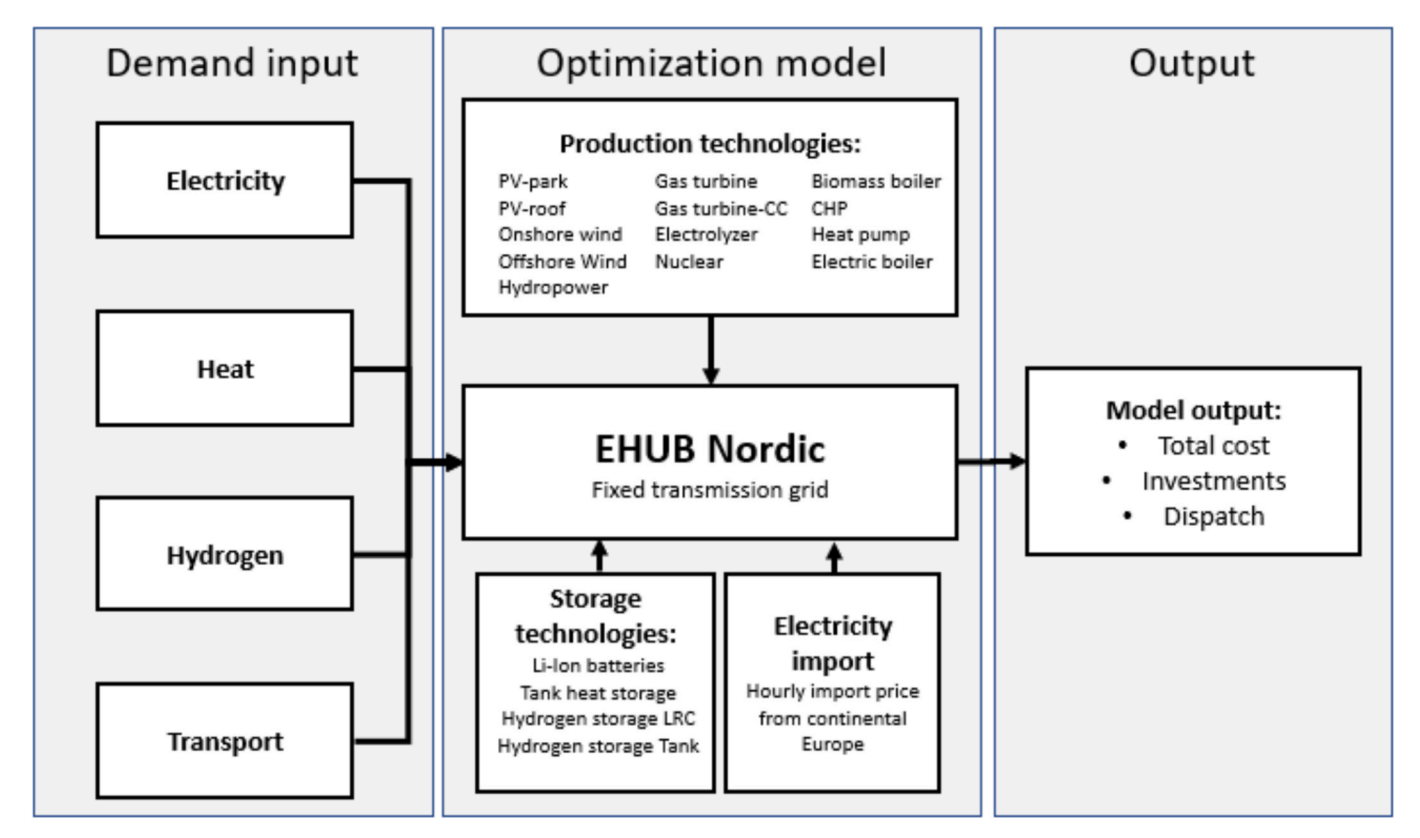


Fig. 1. An overview of the main components in the EHUB Nordic model.

electricity $(p_{i,t,n})$ plus the discharge from stationary batteries $(b_{t,n}^{dch})$ and electricity imported from continental Europe $(w_{t,n}^{imp})$.

A similar equation can be written for the heat balance:

$$D_{t,n}^{heat} + tes_{t,n}^{ch} \le tes_{t,n}^{dch} + \sum_{i \in I_n} q_{i,t,n} \forall t, n$$
(3)

Here, the fixed hourly heat demand $(D_{t,n}^{heat})$ plus the charging of thermal energy storage $(tes_{t,n}^{ch})$ is always less than or equal to the sum of the produced heat $(q_{i,t,n})$ plus discharge from storage $(tes_{t,n}^{dch})$ for each timestep and node.

Similarly, for hydrogen:

$$D_{t,n}^{H2} + h2store_{t,n}^{ch} \le h2_{t,n}^{el} * \eta_{H2} + h2store_{t,n}^{dch} \forall t, n$$
 (4)

This ensures that the sum of the hydrogen demand $(D_{t,n}^{H2})$ plus the charging of hydrogen storage units is less or equal to the produced hydrogen $(h2_{t,n}^{el} * \eta_{H2})$ plus discharge from hydrogen storage $(h2store_{t,n}^{elch})$, for each node and timestep. Thus, neither hydrogen nor heat can be transported between nodes.

2.1.1. Geography and transmission grid

The area to which the model is applied is shown in Fig. 2, together with the geographic resolution, which is based on the locations of the transformer stations (\geq 220 kV) across the Nordic region, based on Year 2023 data from ENTSO-E [35]. The model does not account for endogenous expansion of transmission grid capacity. Instead, it incorporates expansions of the grid based on estimates from the Nordic TSO's [3637], planned to be operational before Year 2040.

Each node included in the model corresponds to a transformer station in the transmission grid, connected to other nodes through an exogenously provided grid (blue lines in Fig. 2). The geographic locations of these transformer stations serve as centroids for generating Voronoi cells that define the geographic areas within the Nordic countries. Consequently, each node is associated with a specific geographic area, from which capacity profiles and production patterns for wind and solar power are derived. The red lines in Fig. 2 illustrate DC links, both

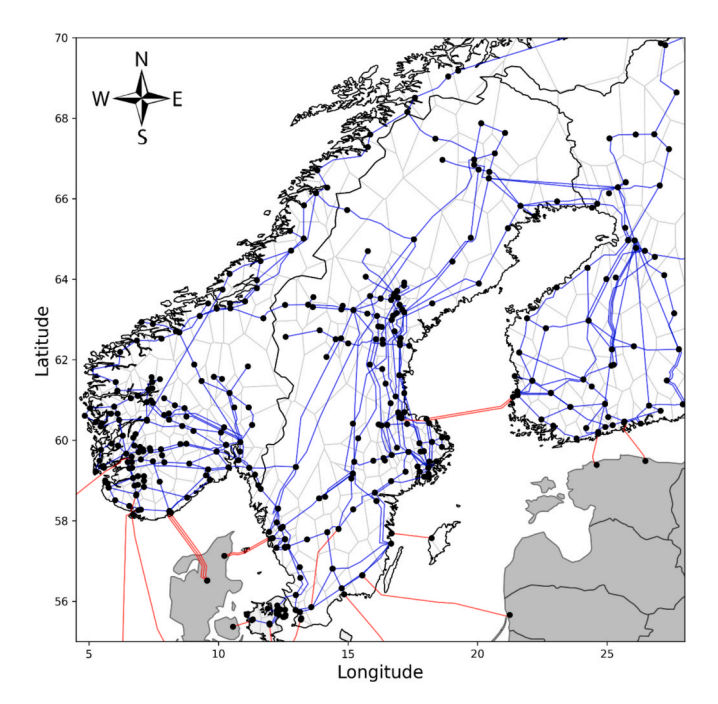


Fig. 2. The geographic area to which the EHUB model is applied, illustrating the Voronoi cells, transmission grid (blue lines) and DC connections (red lines). Gray color indicates areas outside the modeled region.

within the nodes in the model and to neighboring countries in Europe.

The transmission grid is modeled according to the DC load flow, also referred to as linearized load flow, as described in [38] and [39]. This linearization of AC load flow is based on the following assumptions:

- Voltage angle difference between the nodes is small, with $\sin(\Delta\theta) \approx \Delta\theta$ and $\cos(\Delta\theta) \approx 0$.
- The voltage magnitude is fixed at a nominal voltage.
- Reactive power flow is ignored.
- Conductance is negligible relative susceptance.

As a result, the power flow between any two nodes (n and m) at all timesteps can be formulated as:

$$f_{t,n,m}^{trans} = B_{n,m} * (\theta_{t,n} - \theta_{t,m}) \forall t, n, m$$
 (5)

where the power flow between two nodes ($f_{t,n,m}^{trans}$) is equal to the susceptance ($B_{n,m}$) of the line connecting the nodes, multiplied by the voltage angle difference between the nodes. The susceptance values for the modeled grid are based on [40] in which the grid is validated using a full AC power flow model.

In addition, the flow between nodes is constrained by the maximum capacities of the grid lines. These capacities are determined by selecting the lowest value from the calculations based on thermal limitations and maximum voltage angle, as defined by Equations (6) and (7):

$$F_{n,m}^{max,thermal} = \sqrt{3} * V_{n,m}^{rated} * I_{n,m}^{rated} * SF \forall n, m$$
 (6)

$$F_{n\,m}^{max,angle} = B_{n,m}^* \Delta \theta_{max}^* SF \forall n,m \tag{7}$$

where $V_{n,m}^{rated}$ and $I_{n,m}^{rated}$ are the rated voltages and currents, respectively, of each line based on a previous publication [40]. The maximum voltage angle difference, $\Delta\theta_{max}$, is set to 30° as the approximation $\sin(\Delta\theta)\approx\Delta\theta$ introduces a small error (less than 2.5% [41]) within this range, as long as the node voltages are not suppressed relative to the assumed nominal voltage [39]. The term SF is a safety factor used for HVAC lines to account for the n-1 security and additional grid load from reactive power, here set at 0.7, in line with similar grid modeling studies [25]. Transformer stations with voltage levels between 220 kV and 400 kV are modeled as grid lines with infinite maximum capacity and a fixed susceptance. Thus, it is assumed that the capacity of the transformer stations between voltage levels does not limit the magnitude of transferable power. Grid losses are assumed to be proportional to the length of the transmission lines, with 5% power loss per 1,000 km of transferred distance based on [42] and [43].

DC links between two nodes within the model (red lines in Fig. 2) are treated as point loads or generators, ensuring that the production at one end of the DC link equals the load at the other end. DC connections to areas outside the modeled region (see red lines to outside regions in Fig. 2) are allowed to have both positive and negative values, representing imports and exports, respectively, and are constrained by a fixed upper limit for maximum capacity without any option for the model to increase this capacity.

The model permits electricity trade with continental Europe through existing interconnections, shown as red lines linking to grey regions in Fig. 2. The hourly prices of imported and exported electricity are derived from a model of the European energy system originally formulated by Göransson et al. [44], and further developed by Öberg et al. [45] to incorporate future industrial electrification projections. This linear investment optimization model applies a greenfield approach to a Year 2050 energy system for northern Europe, assuming zero fossil CO₂ emissions. The model includes projected future electricity, heat, and transportation demands, and is run using Year 2019 weather data to align with the demand patterns used in this study. The resulting long-term marginal costs of electricity, used in the model as the import/export price for each externally connected bidding zone, are based on a

generation mix that is dominated by wind, nuclear, and solar PV power.

2.1.2. Available technologies

Table 1 illustrates the assumed technical lifetimes, investment costs and efficiencies of the available technologies in the model. Investment costs and lifetimes are based on estimates for Year 2040, taken from Danish Energy Agency [46] if not otherwise stated in the table. Nuclear capacity is limited to nodes with already existing nuclear power production.

2.1.3. Varying renewable electricity production

The model allows for investments in renewable electricity technologies, including onshore wind (WON), offshore wind (WOFF), PV parks (PVP), and rooftop PV (PVR). The production levels from these sources are constrained by both their hourly capacity factors and the available suitable land in each node, following the methodology outlined in [49]. Data for hourly capacity factor profiles are derived from ERA5 reanalysis data. The hourly wind speeds in ERA5 are bias-corrected using the annual average wind speeds from the Global Wind Atlas at high geographic resolution (250 m).

The maximum installable capacity for each VRE technology at each node is determined by the available land area, factoring in restrictions such as built environments and protected areas. Areas with low resource endowment are excluded (annual average 100-m wind speeds <6 m/s

Table 1
Overview of data for technologies included in the EHUB Nordic model. Investments costs are specified in Year 2020 monetary value

Technology	Technical Lifetime (Years)	Investment Cost (EUR/kW)	Efficiency
Production technologies			
Onshore wind	30	1090	-*
Offshore wind	30	1680	-*
Solar PV park	40	320	-*
Solar PV roof	40	699	-*
Reservoir hydropower	-	-	-*
Hydropower run of river with pondage	-	-	_*
Gas turbine biogas	25	575	0.42
Combined-cycle gas turbine biogas	25	866	0.59
Combined-cycle (back- pressure) gas turbine biogas	25	1222	0.51, alpha=2
Nuclear (based on [47])	60	6181	0.33
Electric boiler	25	60	1
Heat pump	25	810	COP=3
Heat only-boiler biomass	20	430	1.15
Heat only-boiler biogas	25	50	1.04
Combined heat and power biomass	25	3360	0.27, alpha=0.4
PEM Electrolyzer	25	500	0.62
Storage technologies			
Lithium ion battery storage	25**	80	1
Lithium ion battery discharge capacity	25	60	1
Tank thermal energy storage	25	3	0.2 %/day loss
Hydrogen storage LRC (Lined rock cavern , based on [48])	30	11	1***
Hydrogen storage Tank	25	29	1***

^{*}Efficiency is included in the production profiles per technology. ** No battery degradation over time is assumed in the model. The 25-year technical lifetime applied is based on the maximum calendar life, rather than the maximum number of cycles. ***Hydrogen storage is associated with no loss, but represents an additional electricity demand for the compressor, corresponding to 12% of the stored energy.

onshore and <7 m/s offshore, or average solar insolation <140 W/m²). After identifying the usable land, a reduction factor [50] is applied to account for other limitations, such as social acceptance and military zones. This adjusted area is then converted to a maximum capacity constraint, based on the power density of each technology. The main assumptions used to generate the data are detailed in Table 2.

2.1.4. Hydropower

Hydropower as of Year 2024 is included in the model as existing capacity, with no further expansion allowed. The operation of all hydropower is limited by the installed maximum capacity in each node according to Equation (8):

$$p_{n,t}^{hydro} \le S_n^{Hydro} \forall n, t \bullet \in Hydro_R, Hydro_RRP$$
 (8)

In addition, the hydropower stations are categorized into two types: Reservoir (Hydro_R), and Run-of-River with Pondage (Hydro_RRP), based on [35]. Hydro_RRP refers to stations located on rivers with relatively small upstream water storage behind the station's weir, making their production and storage levels dependent on the operation of upstream power plants. Reservoir hydropower is, in contrast, modeled as operating independently of other hydropower nodes. This distinction is important because a significant portion of the installed hydropower capacity in the studied region, particularly in Sweden and Finland, is of the Hydro_RRP type, which offers less operational flexibility compared to Hydro_R.

2.1.4.1. Reservoir hydropower. Data for Hydro_R are based on the European Commission's Joint Research Centre Hydropower plants database [51], in terms of installed maximum capacity, storage, and annual expected production. The storage balance for nodes with Hydro_R can be formulated as:

$$l_{n,t}^{hydro} = l_{n,t-1}^{hydro} - p_{n,t}^{hydro} + W_{n,t}^{local} * M_n^{hydro} \forall t, n \in Hydro_R$$
(9)

where $l_{n,t}^{hydro}$ represents the water storage level at each bus per timestep, measured in GWh. The storage level at any given timestep must equal the storage level from the prior timestep $l_{n,t-1}^{hydro}$ minus the hydropower production $p_{n,t}^{hydro}$, plus the local water inflow to the storage $(W_{n,t}^{local})$, which is multiplied by an energy conversion factor (M_n^{hydro}) , to convert water flow into energy flow, as expressed in Equation (10):

$$M_{n}^{hydro} = \frac{P_{n}^{hydro}}{\sum_{t \in T} W_{n,t}^{local}} \forall n \in Hydro_R, Hydro_RRP$$
(10)

where P_n^{hydro} refers to the exogenously determined, expected annual hydropower production volume for each node, while $W_{n,t}^{total}$ represents

Table 2Excluded land types, reduction factors and power densities for the varying renewable energy sources included in the model.

Technology	Excluded land types	Reduction factor	Power density (MW/km²)
Onshore wind	Highly populated areasProtected areasWetlands	0.05	5
Offshore wind	 Protected areas Water depth >40 m Water too near shore (within 5 km) 	0.33	8
Solar PV park	 Highly populated areas Protected areas Forests	0.05	45
Solar PV roof	Sparsely populated areasAll areas not roof	0.05	45

the total inflow of water per node and timestep. The water inflow profiles per timestep are based on Swedish hydropower data [52,53].

In addition, the storage level at any timestep must not exceed the available maximum storage capacity for the node, as defined by Equation (11). This constraint applies to both Hydro_R and Hydro_RRP:

$$c_n^{hydro_store} \ge l_{n.t}^{hydro} \forall n \in Hydro_R, Hydro_RRP$$
 (11)

2.1.4.2. Run of river hydropower with pondage. Run-of-river hydropower (Hydro_RRP) nodes are limited by the same constraints on maximum production and storage capacities, as in Equations (8) and (11). The operation is also limited by a minimum production level constraint equal to 10% of the installed maximum capacity (S_j^{Hydro}) , to account for minimum flow regulations for rivers, as shown in Equation (12):

$$p_{n.t}^{hydro} \ge S_n^{Hydro} * 0.1 \forall t, n \in Hydro_RRP$$
 (12)

In addition, the storage balance of RRP nodes will depend on the operation of upstream nodes in the same river, as the total inflow of water will be a product of both the river inflow and local inflow. Thus, the storage balance for RRP nodes can be written as:

$$l_{n,t}^{\textit{hydro}} = l_{n,t-1}^{\textit{hydro}} - p_{n,t}^{\textit{hydro}} + V_{n,t}^{\textit{local}} * M_n^{\textit{hydro}} + \left(p_{n-1,t-1}^{\textit{hydro}} * \frac{M_n^{\textit{hydro}}}{M_{n-1}^{\textit{hydro}}} \right) \forall t, n \in \textit{Hydro_RRP}$$

(13)

Equation (13) is similar to that describing the storage balance for Hydro_R nodes [Equation (9)], with the only difference being the addition of the expression in the last parenthesis representing the inflow of water from the upstream node in the same river. Here, $p_{n-1,n-1}^{hydro}$ is the production from hydropower in the previous timestep in the upstream node (n-1) while the ratio $\frac{M_n^{hydro}}{M_{n-1}^{hydro}}$ relates to the electricity production potential in nodes n and n-1, according to Equation (10). Thus, this factor accounts for the fact that the value of water varies along the river dependent especially on available head.

As the coupling of production patterns between nodes in the same river increases the computational load, clustering to reduce the number of Hydro_RRP nodes was carried out according to the following principles

- Hydro_RRP nodes connected in series in the transmission grid are aggregated:
- Univalent Hydro_RRP nodes (dead-ends) are merged until only one such node in a branch remains;
- Only nodes within the same bidding zone are clustered; and
- Only nodes in the same river are clustered.

2.1.5. Dispatchable thermal electricity generation

All thermal generation of electricity $(p_{i,t,n})$ per timestep, including nuclear generation, is limited by the installed capacity of each technology i at each node $(s_{i,n})$ according to Equation (15):

$$p_{i,t,n} \le s_{i,n} \forall i \in I_{thermal} \tag{15}$$

Thermal production is associated with both part-load costs and start-up costs, so as to discourage unnecessary cycling whilst keeping the model formulation linear, similar to the implementation in [44]. The variable part-load cost, $(c_{i,t,n}^{part_{load}})$, is calculated from the difference between the production in operation (spinning) $(v_{i,t,n}^{spin})$ and the actual current production level $(p_{i,t,n})$, for each timestep and technology. This cost is multiplied by a fixed cost associated with deviating from the nominal load, $(C_t^{partload})$, which is determined by the efficiency of each technology at part-load), as expressed by Equation (16):

$$c_{i,t,n}^{part_{load}} = C_t^{part_{load}} * (v_{i,t,n}^{spin} - p_{i,t,n}) \forall i \in I_{thermal}$$
(16)

Similarly, all thermal production is associated with a start-up cost $(c_{i,t,n}^{start})$ that is calculated based on how much thermal production capacity is started per node and timestep $(v_{i,t,n}^{on})$, multiplied by a fixed start-up cost per technology (C_r^{start}) , according to Equation (17):

$$c_{i,t,n}^{start} = C_t^{start} * v_{i,t,n}^{on} \forall i \in I_{thermal}$$
(17)

The value for $v_{i,t,n}^{on}$ is added to $v_{i,t,n}^{spin}$ after start-up, to track the operational status of thermal units. In addition, the operation of thermal units is constrained by start-up times, which means that the time that elapses between shutting down and restarting a thermal plant must exceed the specified start-up time for that particular technology. This ensures that thermal units cannot be cycled on and off too quickly, adhering to the technology's operational limitations.

This implementation of thermal production models each technology at each node as a single production unit, without an absolute constraint on minimum capacity. By maintaining a linear structure, the model significantly reduces the computational time while still capturing the key operational flexibility limitations of thermal units.

Since fossil CO_2 emissions are not permitted in the model, gas turbines are only allowed to operate on biogas (hydrogen blending is not included as a technology option). The cost of biogas is calculated based on an assumed biomass price of 40 EUR/MWh, with additional costs for capital depreciation and operation derived from a 200 MW commercial biogas plant, as referenced in [54]. This results in a biogas cost of 77 EUR/MWh, which is applied in this study.

2.1.6. Heat generation

Heat production $(q_{i,t,n})$ from incineration is governed by the same constraints as outlined in Equations (15)–(17). In addition, heat can be supplied by heat pumps (HP) and electric boilers (EB). Heat pumps are assumed to operate with a Coefficient of Performance (COP) of 3 throughout the year, a conservative estimate that is chosen deliberately to avoid overestimating their performance.

2.2. Demand data and modeling

Each node in the EHUB Nordic model is associated with an exogenously predetermined demand for the three energy carriers – electricity, heat, and hydrogen – within the modeling framework. This local demand is derived from four input demand categories: historic electricity demand; heat demand; transport demand; and future industrial demand.

2.2.1. Traditional electricity demand

The traditional electricity demand profile in the model, based on historic data, is derived from measured hourly data for each bidding zone in Year 2019, sourced from the ENTSO-E Transparency Platform [55]. Thus, all the modeled nodes within the same bidding zone have the same demand profile. To determine the magnitude of the annual electricity demand of each node in the model, annual municipal electricity consumption data were used. Municipalities were divided into $1\!\times\!1$ km grid cells, with each cell being assigned an electricity demand proportional to its share of the total land area in the municipality. These grid cells were then mapped to the corresponding Voronoi cells (one per node in the model), to calculate the aggregated electricity demand for each node. Traditional electricity demand data are assumed to remain unchanged when looking at future scenarios and are included as a constant parameter.

2.2.2. Heat demand

Heat demand profiles for district heating are derived from measurement data collected from four different district heating companies located throughout the modeled region for weather Year 2019. Each

bidding zone is assigned one of these profiles according to geographic proximity. The total annual heat demand for each bidding zone is based on national statistics and is assumed to be the same as the Year 2019 level. The allocation from the bidding zone level to individual nodes within the bidding zone is assumed to be proportional to the population size.

2.2.3. Electricity demand for transportation

The model includes the electricity demand from the transportation sector, covering cars, buses, and trucks. It assumes that by Year 2050, the total fleet size in each bidding zone will be the same as in Year 2019, albeit fully electrified. The distribution of electric vehicles from bidding zones to individual Voronoi cells is based on population proportionality. No vehicles are assumed to have the capability for flexible charging or participation in vehicle-to-grid (V2G) discharging. This conservative assumption is adopted to avoid overestimating the transport sector's contribution to system flexibility. The charging patterns for EVs are modeled according to the methodology of Taljegård et al. [56].

2.2.4. Industrial electricity demand

In addition, planned industrial facilities have been manually added to their proposed geographic locations, based on available estimates [57–63]. The industrial processes included were selected for their anticipated key roles in the electrification of industry within the studied geographic region. Table 3 provides an overview of the future industries incorporated into the optimization, and outlines how they are modeled.

2.3. Scenario description

Given the significant uncertainties surrounding the future electricity demand in terms of timing, magnitude, and geographic distribution, two electrification scenarios are analyzed: High Demand and Moderate Demand. The assumptions made regarding the future electricity demand under each scenario are outlined in Table 4. These values exclude endogenously generated demands in the model, such as power-to-heat, grid losses, and trade with continental Europe. As shown, the projected demand in the High Demand scenario is significantly higher than in the Moderate Demand scenario, especially for flexible demands, such as hydrogen production. Fig. 6 illustrates the geographic distribution of the annual net demand for the two scenarios. Here, 'annual net demand' refers to the annual demand remaining after subtracting the existing levels of hydropower and nuclear production at each node. This should not be confused with the concept of 'net load', which describes the residual demand after accounting for production from variable renewables. For both modeled scenarios, no emissions of fossil CO2 are permitted.

Fig. 3 shows that most of Finland and Denmark, along with southern Sweden and Norway's coastline, are dominated by nodes with positive

Table 3Types of industrial demands included in the model and how they are implemented.

Type of industry	Implementation of demand in EHUB Nordic model
Fertilizer	Flexible hydrogen production. For details, see Supplementary
	S1: Modeling of industrial processes.
Electrofuel and	Flexible hydrogen production. For details, see Supplementary
refineries	S1: Modeling of industrial processes.
Plastic	Flexible hydrogen production. For details, see Supplementary
	S1: Modeling of industrial processes.
Steel (HBI	Constant HBI demand to direct reduction shaft, with flexible
production)	hydrogen production and storage. For details, see
	Supplementary S1: Modeling of industrial processes.
Steel (EAF	Flexible EAF operation, with HBI storage. For details, see
operation)	Supplementary S1: Modeling of industrial processes.
Battery	Constant demand
Server halls	Constant demand
Others	Constant demand

Table 4
Future electricity demand per category exogenously provided to the model, as applied to the Nordic region (excluding Iceland). The table does not include endogenously created demands in the model from power-to-heat, grid losses or electricity exports.

Type of demand	Resulting demand [TWh]		
	Moderate Demand scenario	High Demand scenario	
Historical electricity demand	368	368	
Future industry – Steel	20	68	
Future industry – Fertilizer	0	5	
Future industry – Batteries	4	4	
Future industry – Refineries and plastics	0	56	
Future industry – Server halls	20	40	
Future industry – Others	5	10	
Transportation – Buses and trucks	24	47	
Transportation – Personal electric vehicles	38	38	
Total exogenous electricity demand	479	636	
Of which is added demand from electrification	111	268	
Of which is hydrogen production in electrolyzers	14	110	
Heat demand	112	112	

annual net demands (red areas). In contrast, regions with existing hydropower production, particularly inland Norway and northern Sweden, exhibit negative annual net demands (blue areas). As the demand shifts from *Moderate* to *High*, areas of larger positive annual net demand emerge, especially in northern Sweden, along Finland's southern coast, and around Sweden's western coast. The presence of existing nuclear power is represented by dark-blue cells in the maps, located in southern Sweden and southern Finland.

3. Results

Fig. 4 presents the annual electricity production levels for the *Moderate demand scenario* and *High demand scenario*, while Fig. 8 illustrates the corresponding installed technology capacities, categorized as Renewable, Thermal, and Storage. In the *Moderate demand scenario*, onshore wind emerges as the dominant source of electricity generation, complemented by exogenously included hydropower and nuclear power (represented by dashed bars in Fig. 4), with smaller contributions from offshore wind and utility-scale solar PV. As the electricity demand increases in the *High demand scenario*, production from all VRE sources increases, with onshore and offshore wind experiencing the largest absolute increase in annual output, while solar PV exhibits the highest relative growth in terms of output. The annual levels of production from nuclear and hydropower remain constant across both scenarios.

Fig. 8 further illustrates that the installed capacity of thermal peaking technologies with relatively low investment costs, such as open-cycle gas turbines, is higher in the *High demand scenario* than in the *Moderate demand scenario*. In terms of storage technologies, battery capacity increases by 35% as demand rises. However, the absolute size of the battery capacity remains small in comparison to those of the lined rock caverns used for hydrogen storage and thermal tank storage. There is a substantial difference in hydrogen storage capacity between the two scenarios (Fig. 8). These results should be interpreted in light of the different levels of additional electricity demand introduced in the two scenarios: 111 TWh/year in the *Moderate demand scenario*, and 268 TWh/year in the *High demand scenario*. Moreover, a significant share of the additional demand in the *High demand scenario* is flexible, primarily due to increased hydrogen consumption, as detailed in Table 4.

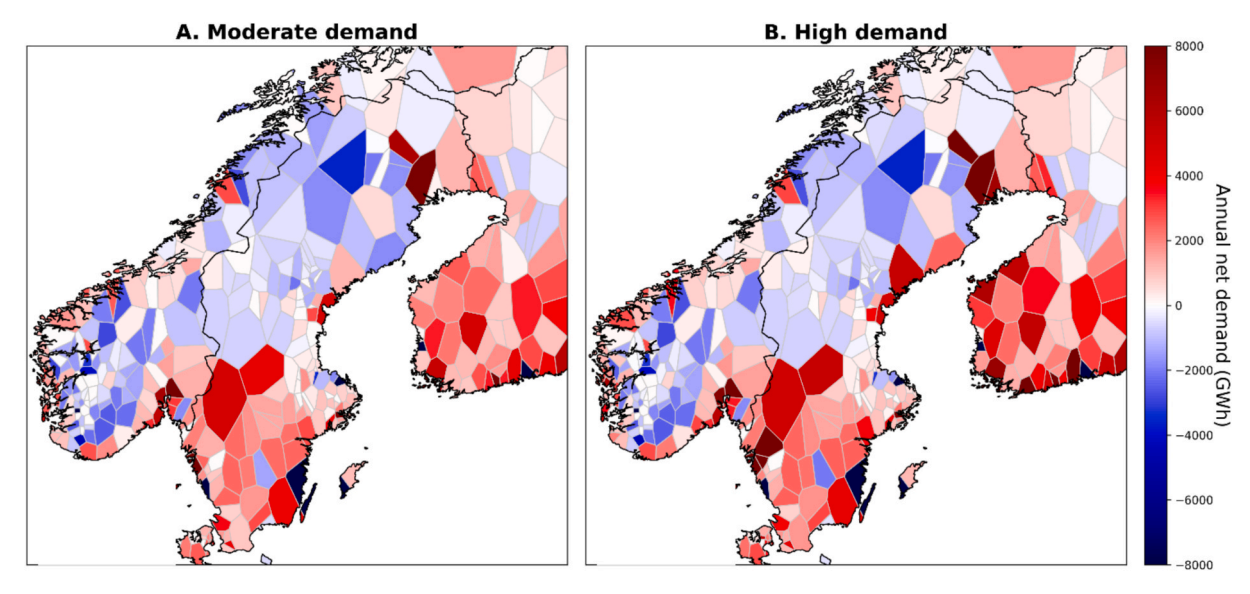


Fig. 3. Annual net demands for electricity of the modeled nodes for the Moderate demand scenario and High demand scenario

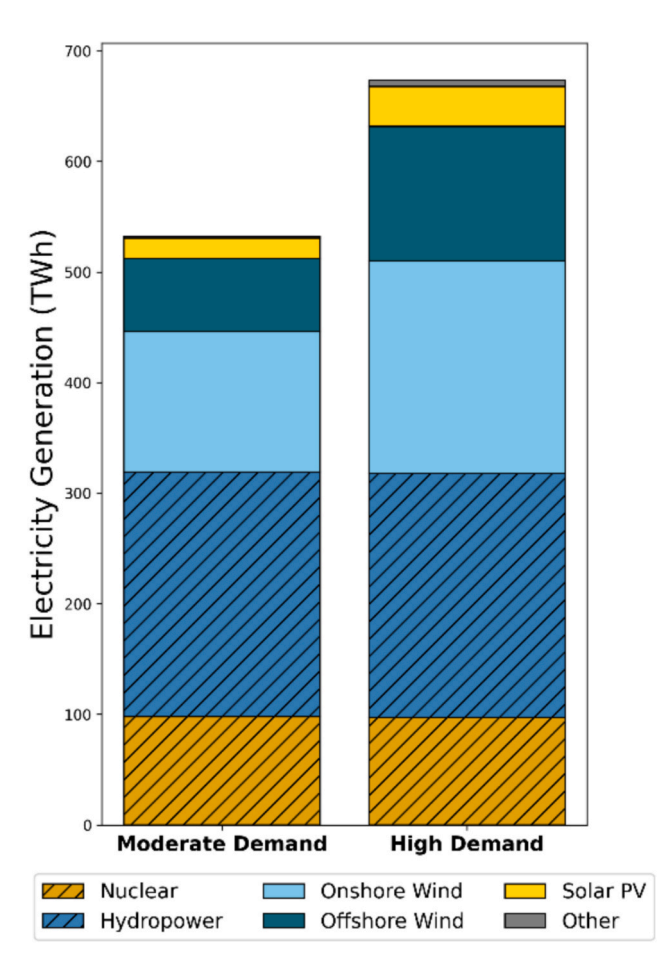


Fig. 4. Annual electricity production levels per technology for the Moderate demand scenario and High demand scenario.

3.1. Optimal localization of onshore wind

As shown in Fig. 5, the optimal installed capacity of onshore wind (as obtained from the modeling) increases from 40 GW in the *Moderate demand scenario* to 63 GW in the *High demand scenario*. The localization of wind power capacity for the two scenarios is illustrated in Fig. 6,

where the color scale indicates the wind conditions expressed in annual full-load hours (FLH) for each node. Since the maximum allowed capacity varies significantly between nodes, the maps display the locations and wind conditions of new production but not the magnitudes of production capacity. A comparison of the two maps reveals that the *High demand scenario* introduces substantially more blue areas, indicating that investing in nodes with high annual production volumes is not always the optimal choice when additional load is introduced into the system. Instead, new onshore wind is concentrated to regions with high annual net demand, as is evident when comparing Fig. 6 and Fig. 6.

The relationship between installed onshore wind and annual net demand is further illustrated in Fig. 7. In this figure, onshore wind installations across all the modeled nodes are plotted against FLH and annual net demand for both the *Moderate demand scenario* and *High demand scenario*. Blue markers indicate nodes where onshore wind is installed. The vertical line marks the boundary between the positive and negative annual net loads, while the horizontal line represents the average number of FLH across all nodes with onshore wind capacity in the model. These two lines divide each plot into four quadrants. The average capacity values shown in each quadrant reflect the average level of utilization of the permitted onshore wind capacity for the nodes falling within that quadrant.

As expected, the highest utilization of onshore wind capacity is found in nodes with high FLH and a positive annual net demand, corresponding to the top-right quadrants in the figures. In fact, all nodes with FLH >3,300 and annual net demand >1,000 GWh/year see investments in onshore wind to the maximum allowed capacity in both scenarios.

In the Moderate demand scenario shown in Fig. 7, a larger share of onshore wind capacity is utilized in the top-left quadrant compared to the bottom-right quadrant. This suggests that, at this demand level, favorable wind conditions play a more-significant role in the optimal placement of onshore wind capacity than proximity to local demand. However, as the demand increases from Moderate to High, this pattern shifts, with most of the new WON production appearing in the bottomright quadrant. This change aligns with the increase in blue areas in the right-hand map of Fig. 6, which suggests that as demand grows and transmission grid congestion increases, proximity to demand becomes a more-critical factor for the optimal siting of onshore wind. This is mirrored by the lower number of average FLH of installed onshore wind in the High demand scenario (2,960 FLH) compared with the Moderate demand scenario (3,100 FLH), despite many sites with higher annual production potential being available, as indicated by the orange circles in the upper half of plot B in Fig. 7.

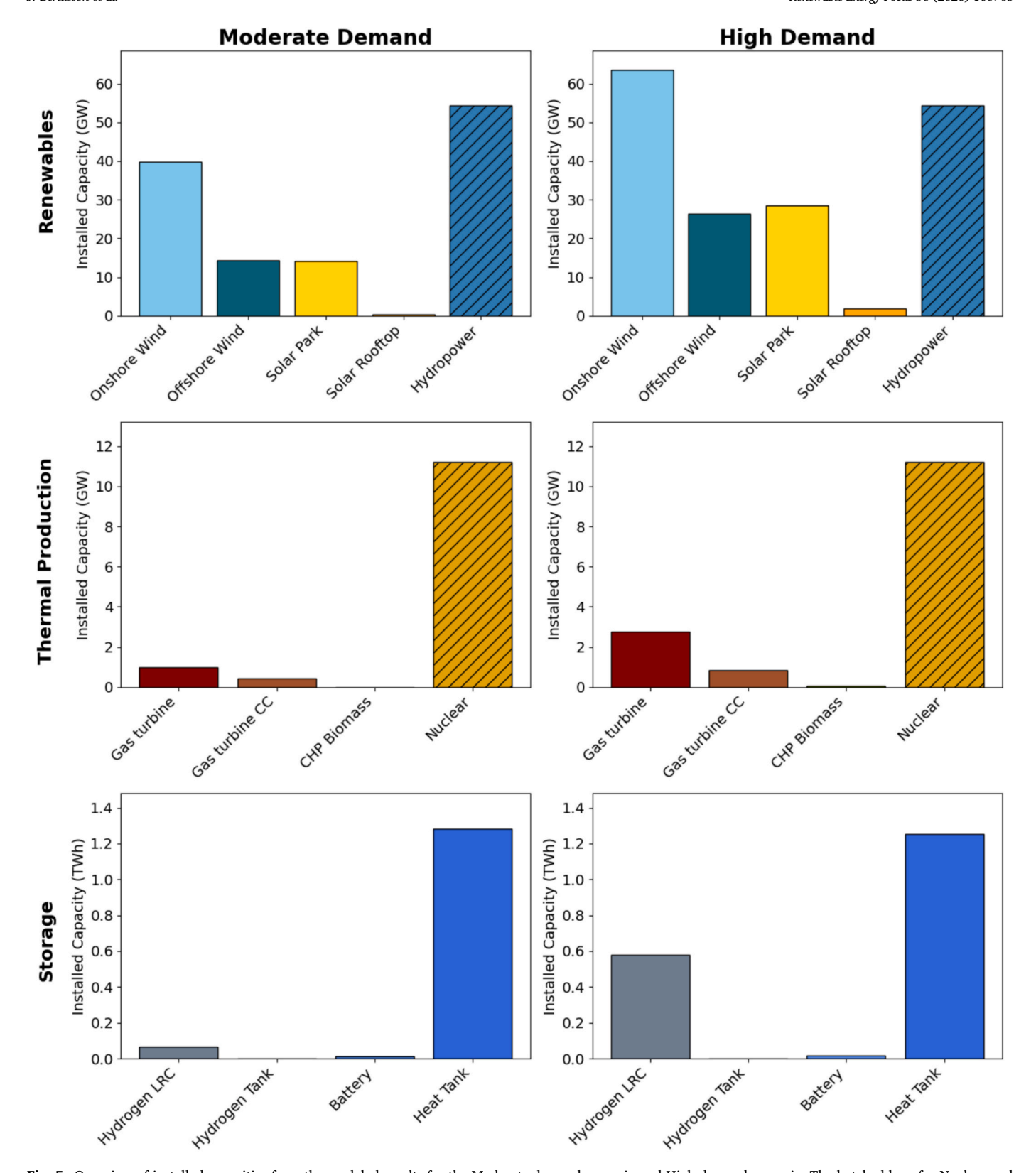


Fig. 5. Overview of installed capacities from the modeled results for the Moderate demand scenario and High demand scenario. The hatched bars for Nuclear and Hydropower indicate that these capacities are not model outputs, but have been exogenously provided to the model. The results are aggregated for the entire modeled region, with the constraint that no fossil CO_2 emissions are permitted.

Deviations from the expected trend of favoring wind power installations in nodes with high annual production and positive net demand are evident in Fig. 7. The area marked as "1" in Fig. 7 highlights investments in nodes that are characterized by poor wind conditions and

negative annual net demand. These deviations are primarily observed in the *High demand scenario*, and can be attributed to the geographic proximity of these nodes to major demand centers, particularly within the two highlighted areas in Fig. 6. Consequently, the modeled cost-

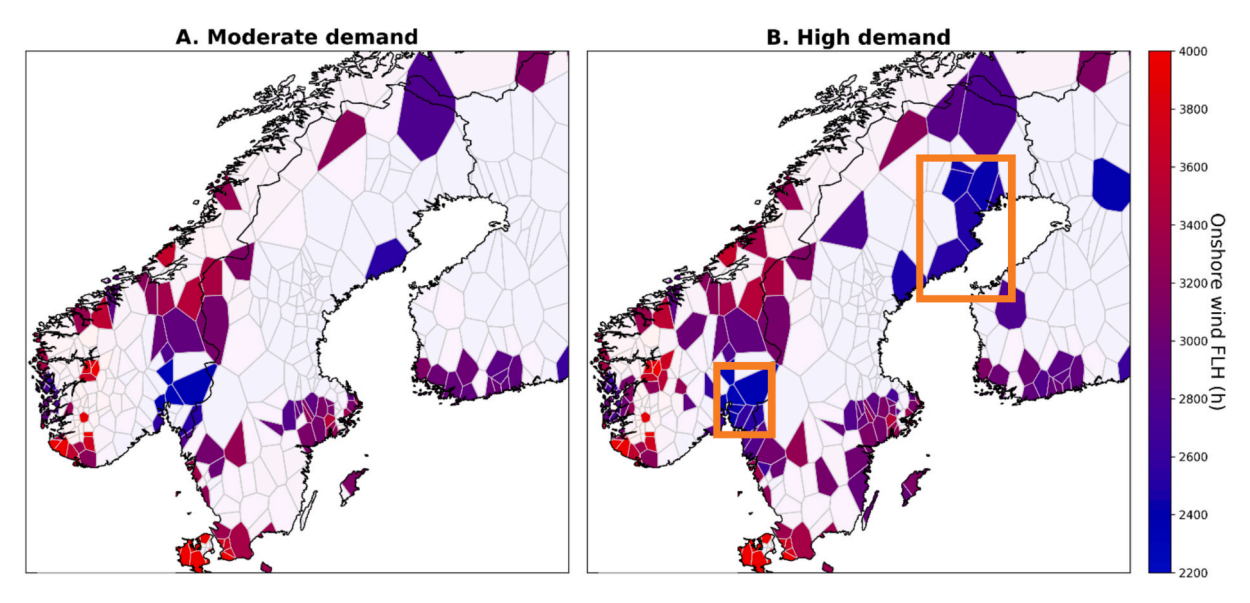


Fig. 6. Geographic localization of onshore wind from the modeled results. Colored cells represent the geographic locations where onshore wind is installed. The color scale indicates the number of full-load hours for offshore wind in each cell with onshore wind. Highlighted areas are referenced in the text.

efficient capacity of onshore wind in these regions appears to be driven by a high regional electricity demand, despite poor wind conditions.

Another deviation from the expected pattern in Fig. 7 is marked as "2" and is present in both the *Moderate demand scenario* and *High demand scenario*. This deviation arises from the colocation of onshore wind (WON) and nuclear power. Despite having low net demands for electricity, as a result of nuclear power production, these nodes are favorable for onshore wind generation due to their strong grid connections and proximity to areas with high annual net demands.

3.2. Optimal localization of offshore wind

Fig. 8 illustrates the optimal siting of offshore wind in both the *Moderate demand scenario* and *High demand scenario*. The maps show the land areas closest to the actual locations where offshore wind parks would be installed. Similar to the depiction of onshore wind power, the cell color reflects the number of annual FLH, albeit with a different scale. Notably, despite an increase in offshore capacity from 14 GW to 26 GW, the optimal siting remains largely consistent across both scenarios. The regions with the highest concentration of offshore wind installations include southern Finland and the northern part of Sweden's west coast.

Unlike onshore wind, higher electricity demand does not lead to the appearance of any new blue cells in the right-hand side map in Fig. 8, indicating minimal investment in areas with low numbers of FLH for offshore wind in any scenario. This pattern is further illustrated in Fig. 9, which demonstrates how offshore wind installations correlate with FLH and the node annual net demand. The plots follow the same structure as described for Fig. 7, with quadrants defined by average FLH and the boundary between positive and negative annual net loads, and the average capacity values displayed for each quadrant.

Here, it becomes clear that the offshore wind investments in both demand scenarios are almost exclusively situated in nodes with favorable wind conditions and positive annual net demands, shown as blue markers in the top-right quadrant. This contrasts with onshore wind, where investments in nodes with less-favorable wind conditions are common, particularly in the *High demand scenario* (cf. Fig. 7). The difference can be attributed to the cost structures of the two technologies, as outlined in Table 4. Thus, offshore wind has a 50% higher investment cost than its onshore counterpart. Consequently, the model only finds offshore wind power to be cost-effective at locations that yield sufficiently high annual numbers of FLH. This is also reflected by the average number of FLH for offshore wind, which remains largely constant

between the two scenarios, with 4,630 FLH in the *Moderate demand scenario* and 4,620 FLH in the *High demand scenario* .

Similar to onshore wind, some deviations from the expected patterns appear for offshore wind in Fig. 9, indicated by numbered circles in the plots. As with onshore wind, colocation with nuclear power (circled as "1" in the plot) promotes offshore wind installations, despite low annual net demands at these nodes, particularly in the Moderate demand scenario when the transmission grid is less-congested. In addition, as indicated by the circles marked as "2" in the plots, several nodes with excellent wind conditions and high positive annual net demands do not see offshore wind installations as part of the optimal solution. These nodes, characterized by annual FLH >4,500 and annual net demands >4,000 GWh, are all located near DC link connections to continental Europe (illustrated in Fig. 2). The prices of electricity imports and exports through these DC links are significantly impacted by a high share of wind-based generation in the surrounding region, leading to overspill effects that reduce the economic attractiveness of offshore wind power in these nodes within the model. Thus, the connection to wind-dominated northern continental Europe lowers the value of wind power in the nodes that lie closest to external DC links.

The third deviation, marked as "3" in Fig. 9, originates from offshore wind power in a node in western Norway, where significant grid congestion occurs. This results in an abnormally high value for local electricity production, which drives offshore wind installations despite comparatively low numbers of FLH.

3.3. Optimal localization of solar PV

The deployment of utility-scale solar PV in the modeled results is presented in Fig. 10 for both the *Moderate demand scenario* and *High demand scenario*. Similar to what is shown in Fig. 5, Fig. 14 further emphasizes that higher demand is associated with significant expansion of solar PV installations, as evidenced by the increased colored areas in map B. Moreover, Fig. 10 reveals a notable shift in the geographic distribution of new PV capacity in the *High demand scenario* compared with the *Moderate demand scenario*. New installations in the *High demand scenario* are primarily concentrated along the coast of Finland, despite these areas having relatively low FLH potential for solar PV. Instead, the spatial distribution appears to be primarily influenced by colocation with positive annual net demand, as suggested by a comparison of Fig. 10 with Fig. 6.

Similar to the analysis conducted for onshore and offshore wind, the

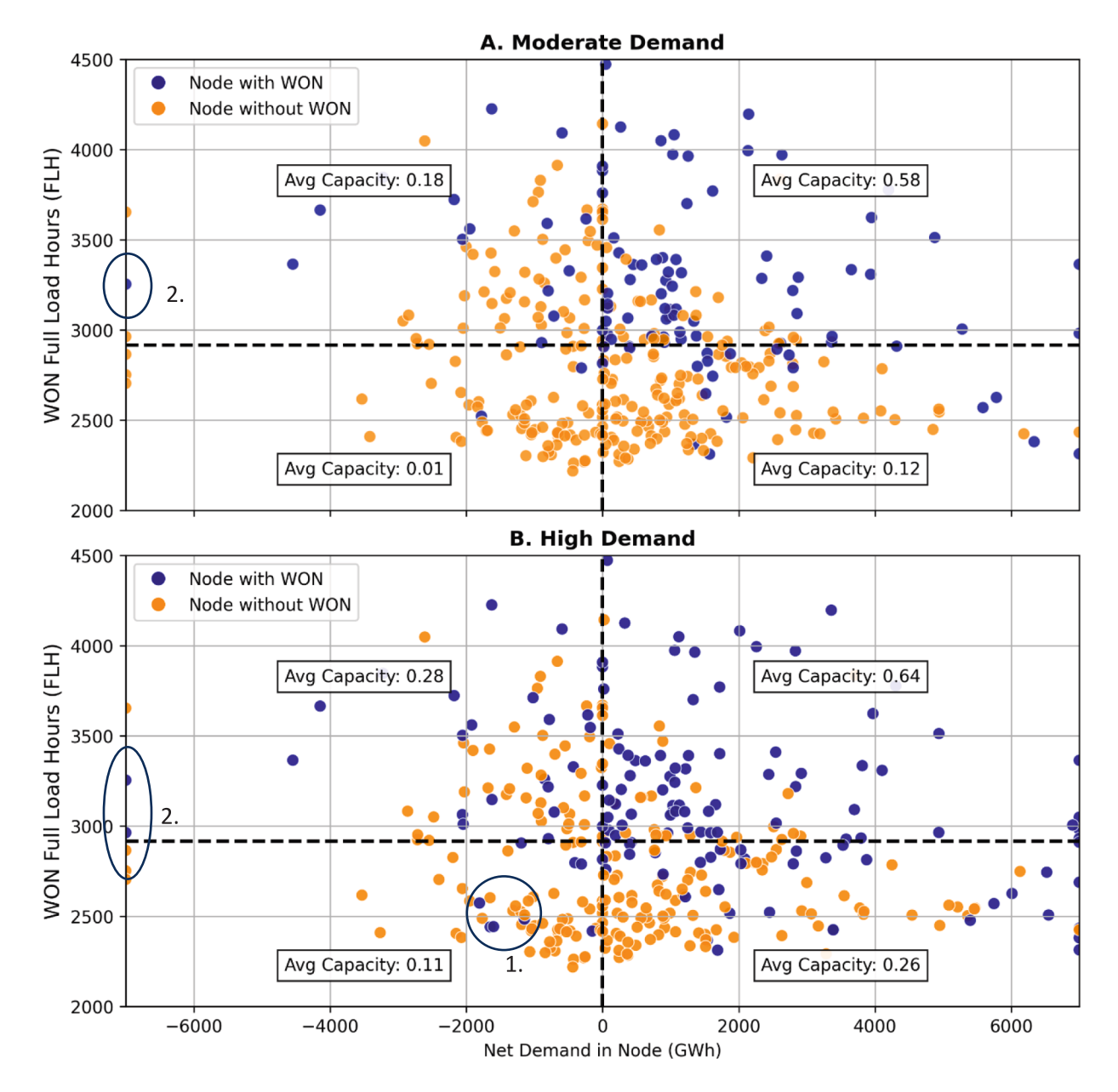


Fig. 7. Scatter plot depicting the installation of onshore wind units in all nodes in the model, plotted against full-load hours (y-axis) and the node annual net demand (x-axis) for the two scenarios. The blue markers indicate that onshore wind is installed in that node. The horizontal dotted line represents the average FLH value of all included nodes, while the vertical line indicates the distinction between positive and negative node annual net demands. The presented Average capacity values represent the average utilized onshore wind capacity for the datapoints located in the respective quadrants. Nodes with zero onshore wind capacity are excluded from the plot. Datapoints outside the diagram limits are included on the outside borders of the plot for visibility reasons. Numbered circles indicate deviating datapoints, as explained in the text.

relationship between FLH and annual net demand for PV installations in the modeled results can be illustrated using a scatter plot (Fig. 11). This figure demonstrates that in the *Moderate demand scenario*, solar PV investments are almost exclusively concentrated in nodes with positive annual net demands and relatively high numbers of annual FLH. One of few exceptions to this, marked with a circle labeled "1" in plot A in Fig. 11, corresponds to a situation with colocation of PV and nuclear power.

With the introduction of increased electricity demand in the *High demand scenario*, most of the new PV capacity is introduced in nodes with positive annual net demands – particularly in areas where the number of annual FLH exceeds the average. In nodes with an annual net demand exceeding 5,200 GWh and above-average number of FLH , PV installations are found to be optimal across all nodes (area marked "2" in

Fig. 11).

Solar PV exhibits the lowest level of investment in nodes with negative annual net demands, when compared with onshore and offshore wind power. In the *Moderate demand scenario*, only 3% of the total PV capacity is allocated to such nodes, increasing slightly to 8% in the *High demand scenario*. This dependency of optimal PV placement should be understood in the context of its production profile, especially when compared with other VRE sources. The diurnal nature of PV production, characterized by high-amplitude and short-duration peaks, makes it less-suitable for long-distance transmission in a grid with limited capacity, particularly under conditions of high demand and heavy grid congestion.

However, certain data-points in the *High demand scenario* appear to deviate from this general trend. These nodes, highlighted as "3" in plot B

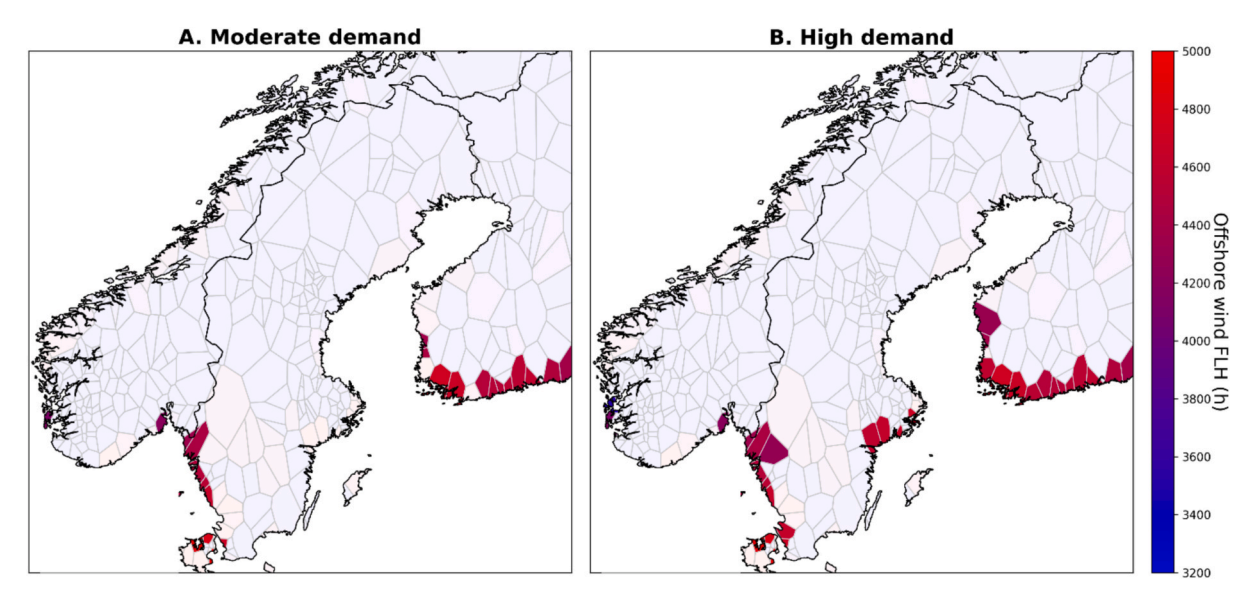


Fig. 8. Geographic localization of offshore wind from the modeled results. Colored cells represent the geographic locations on the coast, outside of where offshore wind is installed. The color scale indicates the number of full-load hours for offshore wind in each cell with installations.

in Fig. 11 for the *High demand scenario*, are situated in close proximity to large demand centers and are connected to positive net demands through a strong transmission grid. Thus, the electricity generated at these locations is consumed in neighboring nodes and can be regarded as part of a localized solution rather than as part of a centralized production system. This is similar to the behavior of onshore wind, illustrated in Fig. 6. Here, regional areas defined by congestion in the transmission grid become associated with a higher value for localized electricity production, thus making the production technology, in this case solar PV, part of the optimal solution despite unfavorable production conditions in terms of FLH.

Only 0.9% of the total solar PV investments from the *Moderate demand scenario* are not included in the optimal solution for the *High demand scenario*, which is a lower share than for onshore wind (2.5%) or offshore wind (6.5%). This suggests that solar PV is the technology whose optimal geographic placement is least-sensitive to increases in the electricity demand at an aggregate level. However, none of the investigated technologies exhibit a strong tendency to shift their optimal localization as new demand centers emerge in the *High demand scenario*. This indicates that decisions regarding the placement of new production technologies can be made with confidence, even in the face of significant uncertainties related to the absolute size of future demand projections.

3.4. Optimal localization of gas turbines and batteries

As illustrated in Fig. 8, the deployment of gas turbines increases the capacity from 1.5 GW to 3.8 GW in the High demand scenario, while battery capacities exhibit a similar expansion, growing from 11 GWh to 15 GWh. Fig. 12 provides a spatial representation of the gas turbines and batteries in the High demand scenario. Similar to wind and solar power, the optimal siting of gas turbines and batteries is influenced by the localization of a high annual net demand for electricity. For instance, regions such as southern Finland, western Norway, and the Oslo area experience significant installations of gas turbines and exhibit high annual net demands for electricity (as shown in Fig. 6). However, exceptions exist, such as in northern Sweden, where despite a substantial net electricity demand, gas turbines and batteries are entirely absent. This absence can be partially attributed to the temporal flexibility of new demand in the region -as in the case of hydrogen production which can be shifted over time and does not necessarily contribute to a new peak demand. Furthermore, northern Sweden benefits from substantial hydropower capacity, which effectively manages fluctuations in the electricity demand.

For nodes that lack hydropower availability, the placement of gas turbines and batteries is strongly correlated with a firm peak demand relative to the node's total import capacity - a metric termed 'peak import congestion'. This metric is calculated by dividing the annual firm peak demand of a node by its total import capacity from neighboring nodes in the transmission grid. Fig. 13 presents the peak import congestion levels across all the modeled nodes in the High demand scenario, sorted in descending order. The upper graph depicts the installed gas turbine capacity per node (red bars), while the lower graph illustrates the magnitude of the installed stationary battery capacity per node (blue bars). Although only the results for the High demand scenario are displayed, similar trends are observed for the Moderate demand scenario. The figure demonstrates that both technologies are predominantly installed in nodes with high peak congestion levels, which are classified as 'locally congested nodes'. In these nodes, the electricity demand cannot be met solely through imports from the transmission grid, indicating that local grid bottlenecks are a key driver of these investments. Around 45% of the total gas turbine capacity and 52% of the capacities of the batteries are associated with such locally congested nodes (with peak import congestion >0.4).

Fig. 13 further indicates that certain nodes with high congestion levels (far to the left-hand side) lack gas turbines and/or batteries. This can be attributed to the availability of hydropower with storage at these locations. Furthermore, some of the largest gas turbine installations – designated as 'regional power deficit nodes' in Fig. 13 – are located in areas with relatively low peak import congestion values (<0.2). These installations, such as those in eastern Finland (depicted in Fig. 16), are primarily driven not by local grid bottlenecks but by regional power deficits. During periods of low wind production and high electricity demand, gas turbines emerge as the most-cost-effective solution for meeting the electricity demands in these regions, particularly where hydropower availability is low. As a result, the highest concentration of gas turbine capacity is observed in eastern Finland, highlighting the necessity to have dispatchable generation in this region.

Another deviation from the expected correlation between peak import congestion and battery installations is observed in the 'solar PV nodes' in Fig. 13. These nodes feature battery installations despite exhibiting low peak import congestion levels. This pattern can be explained by comparing Fig. 12 and Fig. 10, which illustrates the optimal siting of solar PV. Batteries in solar PV nodes, for example in southern Finland and the Oslo region, are primarily deployed to manage

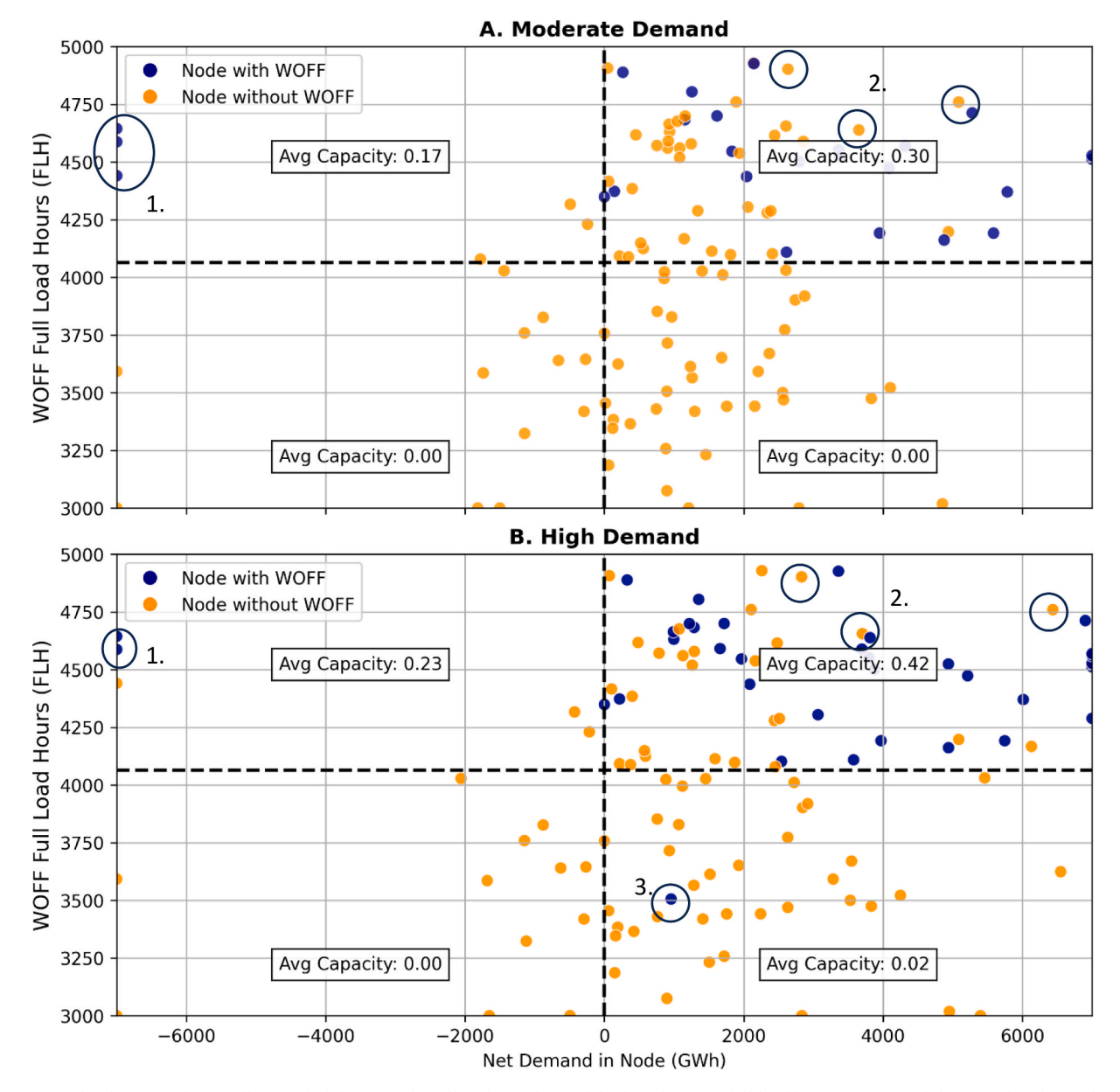


Fig. 9. Scatter plot depicting the installation of offshore wind in all nodes in the model, plotted against full-load hours (y-axis) and the annual node net demand (x-axis). The blue markers indicate that offshore wind is installed in that node. The horizontal dotted line represents the average FLH value for all the included datapoints, while the vertical line indicates the distinction between positive and negative annual node net demands. The presented Average capacity values represent the average utilized offshore wind capacity for the datapoints located in the respective quadrants. Nodes with zero offshore wind capacity are excluded from the plot. Datapoints outside the diagram limits are included on the outside borders of the plot for visibility reasons. The numbered circles indicate deviating datapoints, as explained in the text.

diurnal variations in solar power generation rather than to mitigate local grid congestion, explaining the strong spatial alignment between battery placement and solar PV locations.

3.5. Sensitivity analysis: reduction of maximum grid line capacity

Throughout this study, a safety factor of 0.7 (referred to as the 'Standard grid capacity') has been applied to reduce the maximum grid capacity values, accounting for factors such as the n-1 criterion and reactive power, in line with similar modeling work [25]. In this sensitivity analysis, a safety factor of 1 (referred to as the 'High grid capacity') is used, meaning that the maximum grid capacities are determined solely by thermal constraints, as described in Section 2.1.1. Since the observed trends are similar in both demand scenarios, the presented results are primarily for the $High\ demand\ scenario$.

Fig. 14 presents the average installed capacities per technology – as a share of the maximum allowed capacity – for the quadrants introduced in Figs. 10, 12, and 14. These quadrants are defined based on whether a node has a positive or negative annual net demand and whether its number of FLH is above or below the average (as indicated by the dashed lines in Figs. 10, 12, and 14). For example, the bars in the top-left quadrant represent the average installed capacities (as a share of the allowed maximum) for all nodes with a negative net demand and above-average FLH, shown separately for offshore wind, onshore wind, and solar PV, under both grid capacity assumptions.

As shown in the figure, expanding the grid capacity leads to a reduction in production capacity in the bottom-right quadrant and an increase in production capacity in the top-left quadrant, indicating a shift towards locations with higher numbers of FLH. This trend confirms that as grid capacity increases, proximity to demand centers becomes a

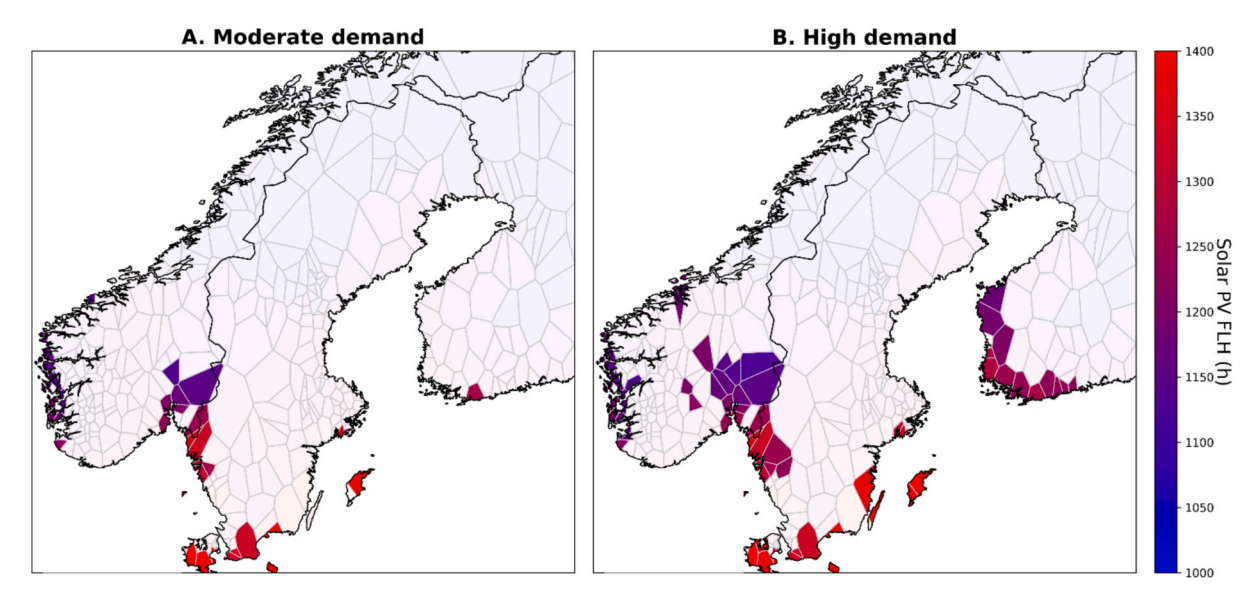


Fig. 10. Installation of utility-scale solar PV in the two modeled scenarios. The color scale indicates the number of full-load hours for offshore wind in each cell that acquires PV installations in the results.

less-critical factor for the optimal siting of wind and solar power generation.

Another key observation from Fig. 14 is that solar PV production capacity decreases with increased grid capacity across all quadrants as it is outcompeted by wind power. The local value of solar PV, which contributed to its penetration level in the *High demand scenario*, diminishes as a higher grid capacity enables more-flexible electricity transfers between nodes. Due to its high-amplitude, high-frequency production variations, solar PV benefits less from a moderate increase in grid capacity compared with onshore and offshore wind power. In contrast, WON and WOFF, with their longer and less-frequent production variations, are better suited to leveraging increased grid capacity, making them more-favorable in the High grid system.

It is also important to emphasize that increasing the grid capacity in the sensitivity analysis leads to a significant relocation of VRE production capacity. This effect is illustrated in Fig. 15, which depicts the share of production capacity that is relocated under two different changes to the modeling inputs: (1) increasing the demand level from Moderate to High; and (2) increasing grid capacity from Standard to High in the *High demand scenario*.

Fig. 15 clearly shows that the results are more-robust to variations in demand levels and more-sensitive to how the electricity grid is represented in the model. This sensitivity is further reflected in the impact on total system cost, illustrated in Table 5. Compared to the Standard grid assumption, total system cost is reduced by 12% in the *High demand scenario* and by 14% in the *Moderate demand scenario* as the grid safety factor is changed from 0.7 to 1. These findings highlight the critical role of grid representation in shaping model outcomes and emphasize the importance of continued evaluation of how the thermal limits of the grid can be utilized more efficiently, for instance through approaches such as dynamic line rating. Table 5 also highlights that the majority of costs are attributed to investments, reflecting the dominance of power sources such as wind and hydropower in the modeled results—technologies characterized by low operational costs.

In terms of installed production capacities, the most-pronounced differences between the High and Standard grid assumptions are observed in the thermal peaking units and battery storage units. Specifically, the installed capacity of open-cycle gas turbines decreases by 42% with increased grid capacity, while battery storage capacity declines by 43%. The enhanced ability to transfer electricity between nodes reduces the reliance on local flexibility solutions, particularly in nodes that are identified as "locally congested" in Fig. 13, underscoring

the strong dependence of these technologies on local grid conditions.

4. Discussion

The results presented in this study represent the optimal spatial allocations of distributed production and storage units from a purely techno-economic perspective. Consequently, considerations related to other aspects, such as political or social factors, are not included. In the studied region, this omission is particularly relevant for offshore wind deployment, where for example military interests may significantly influence site selection. Furthermore, the model uses a simplified representation of social acceptance for renewable energy deployment. The impact of social acceptance is applied through a reduction factor to limit available land use, considering for example population density and protected areas. However, it does not account for the phenomenon in energy system modeling whereby high geographic resolution can lead to solutions that incorporate highly spatially concentrated deployment of wind and solar power, which may be socially unacceptable [64].

For example, the results for onshore wind indicate a preference for deployment of wind power in areas with high annual net electricity loads, such as Oslo, Stockholm, and Copenhagen, as shown in Fig. 6. These locations are densely populated, raising concerns about the practical feasibility of the proposed siting. Lohr et al. [64] have explored this issue in detail, demonstrating that incorporating quadratic environmental costs, which penalize high shares of the maximum allowable capacity for renewables in a region, could be an alternative approach to this problem, albeit at the expense of a higher computational burden.

Previous research has also demonstrated that high spatial resolution in energy systems modeling influences the optimal production mix, primarily by preserving high FLH sites that would otherwise be diluted in aggregated models. This effect tends to favor onshore wind over offshore wind and solar power, aligning with the findings of this study, where onshore wind emerges as the dominant new electricity source. However, as electricity demand increases, a significant share of the onshore wind capacity is deployed in areas with comparatively poor wind conditions, suggesting that the availability of high-quality sites identified using the high-resolution approach eventually becomes saturated. Instead, the results underscore the growing importance of colocalization with regions of high annual electricity demand, particularly for onshore wind and solar power, as demand levels rise.

The applied model consists of 352 nodes distributed across 11 bidding zones. The results presented in this study are derived from an

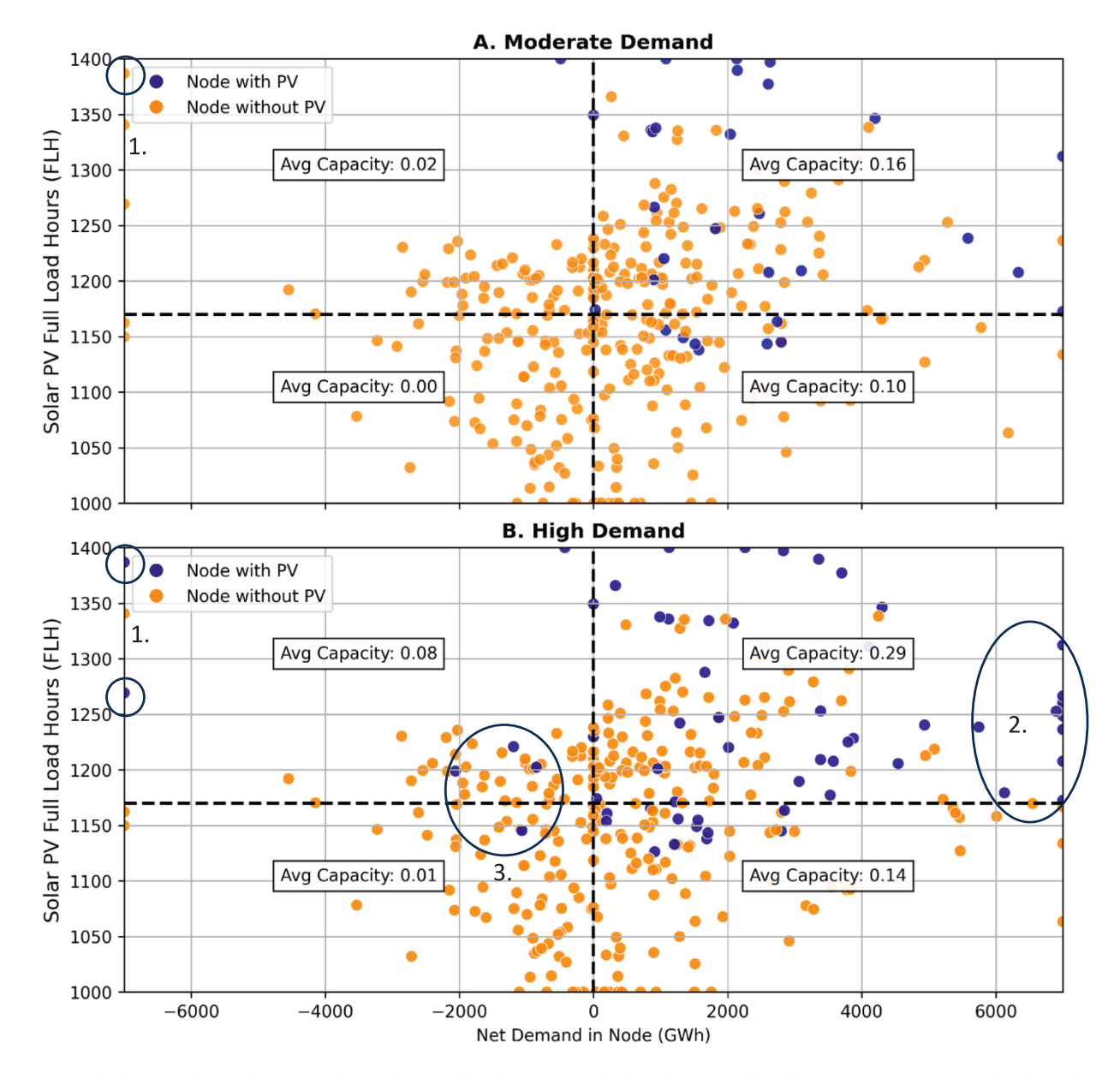


Fig. 11. Scatter plot depicting the installation of utility-scale PV in all nodes in the model, plotted against full-load hours (y-axis) and the annual node net demand (x-axis). The blue markers indicate that PV is installed in that node. The orange markers indicate that there are no PV installations. The horizontal dotted line represents the average FLH value of all the included datapoints, while the vertical line indicates the distinction between positive and negative annual node net demands. The presented Average capacity values represent the average utilized PV capacity for the datapoints located in the respective quadrants. Nodes with zero PV capacity are excluded from the plot. Datapoints outside the diagram limits are included on the outside borders of the plot for visibility reasons. The numbered circles indicate deviating data-points, as explained in the text.

optimization framework that determines the placement of production and storage units based on the total cost of the 352-node system, rather than the electricity valuation mechanisms inherent to the bidding zones. Consequently, discrepancies may arise between the price signals at the bidding zone level and those at the nodal level. Achieving alignment between economic incentives and the optimal localization of production, as suggested by this study, will necessitate a more-granular approach to electricity valuation. In an extreme scenario, this would imply the establishment of 352 bidding zones in the Nordic region. While such an approach is neither practical nor desirable, it underscores the limitations of the current bidding zone structure in incentivizing optimal production plant placement. This observation is consistent with previous research, such as the work of Obermüller [34], which has demonstrated that zonal pricing mechanisms that fail to account adequately for grid constraints may result in inefficient locational

signals for VRE generation.

The model's calculations of the flexibility requirements for technologies such as gas turbines and batteries are subject to both under- and over-estimation due to the assumptions applied. On the one hand, the model's 3-hour temporal resolution may smoothen fluctuations in generation and demand, potentially leading to an underestimation of the need for short-term flexibility measures. On the other hand, the model adopts a conservative assumption that the transportation sector does not contribute to system flexibility through either vehicle-to-grid discharge or flexible charging. Furthermore, the model does not incorporate additional functionalities such as participation in ancillary service markets or black-start capabilities.

A further limitation of this analysis is that investment decisions are based on a single representative weather year. As shown in the studies carried out by Zeyringer et al. [65] and Bloomfield et al. [66], the choice

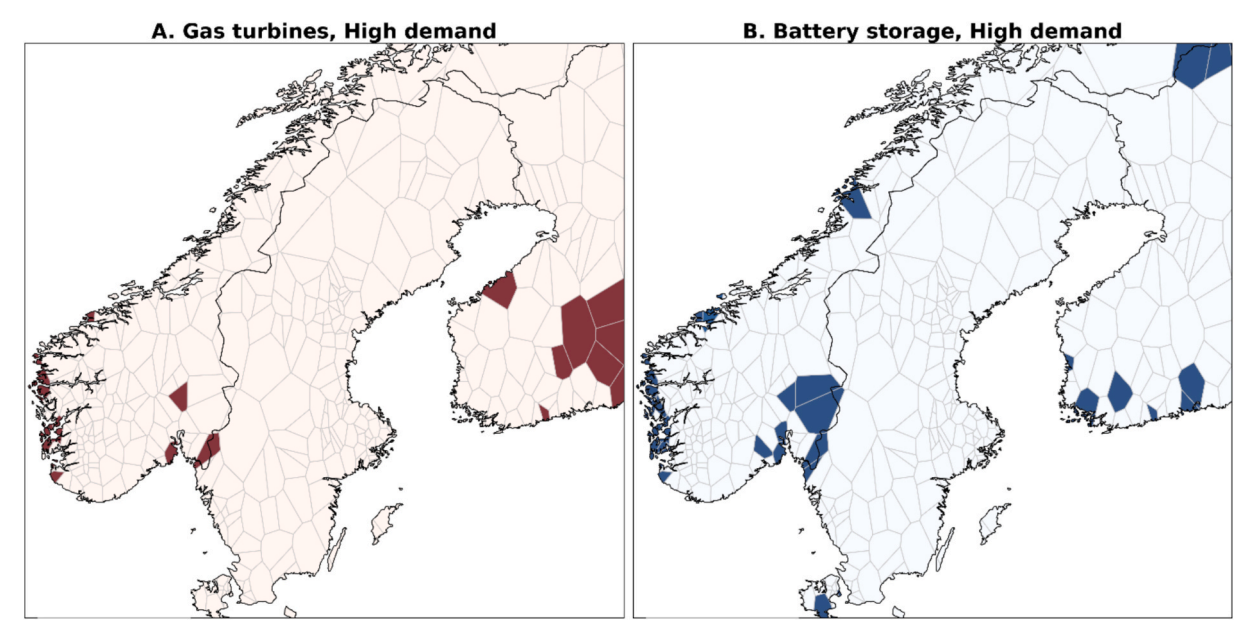


Fig. 12. Geographic positions of installed batteries (to gas turbines in open and combined cycle for the High demand scenario.

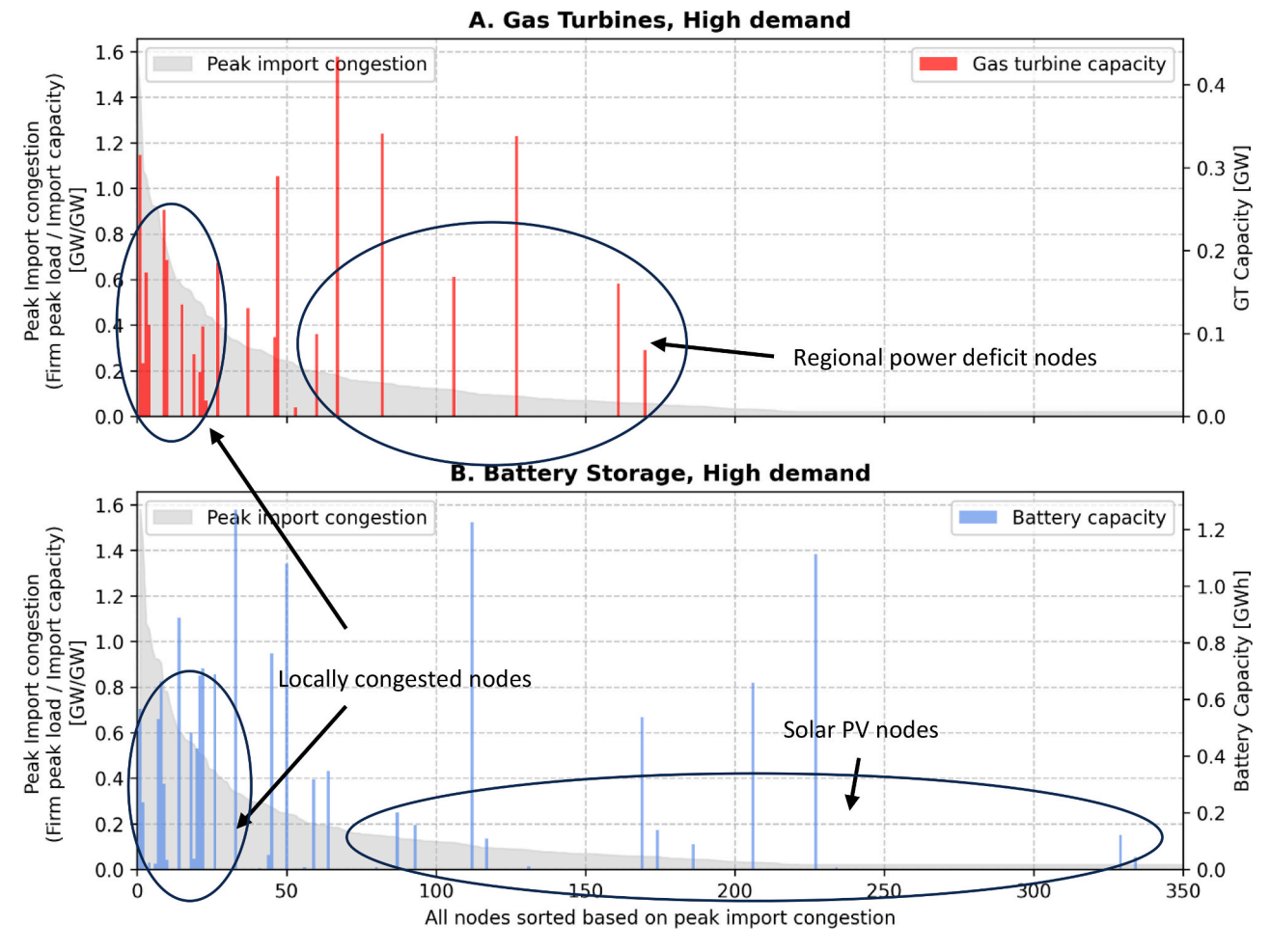


Fig. 13. Congestion levels for all nodes in the model for the High demand scenario, sorted from high to low. The red bars indicate gas turbine installations in each node. The node congestion level is calculated for each node by taking the highest annual inflexible demand value (firm peak load) and dividing it by the total electricity import capacity to the node.

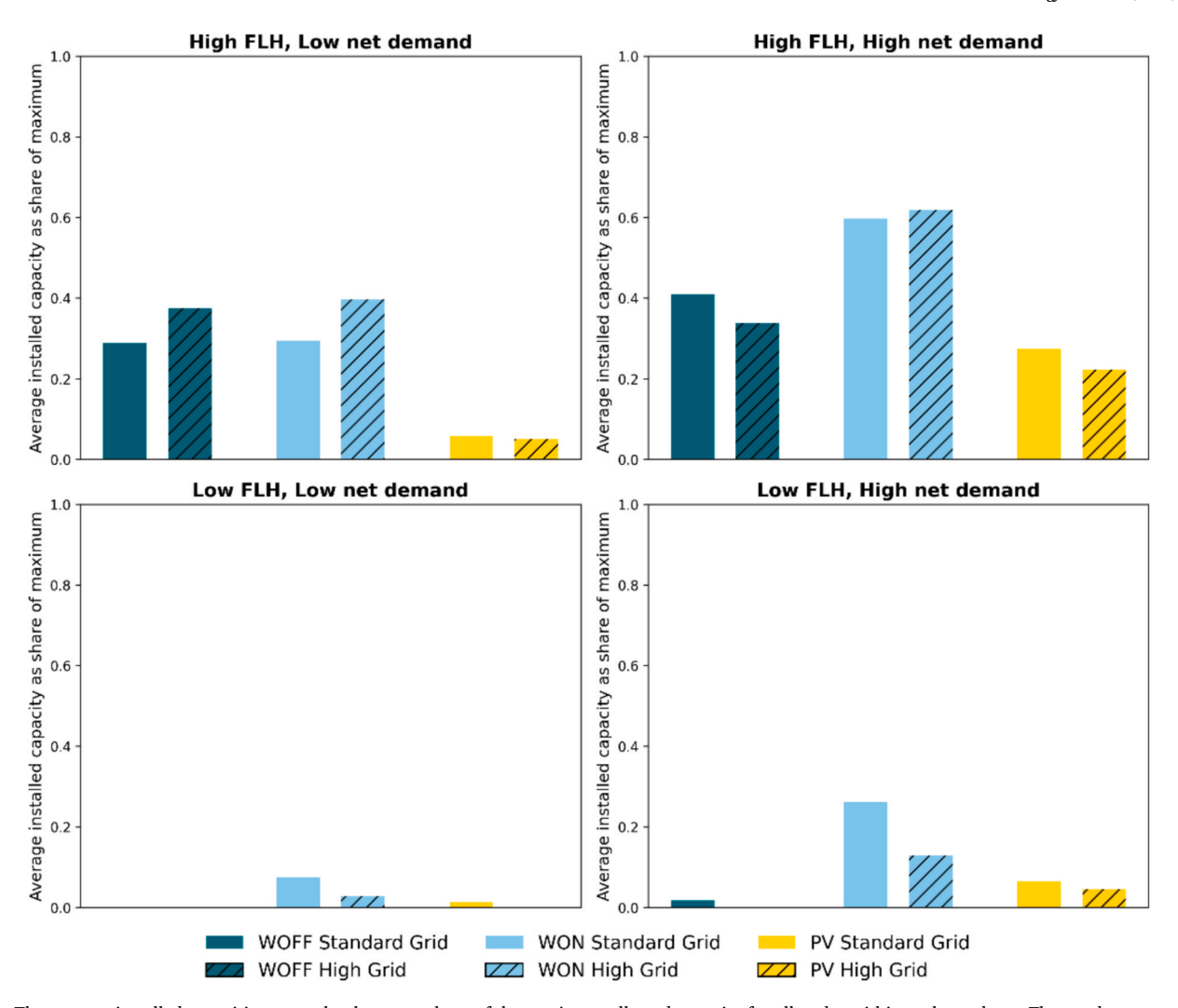


Fig. 14. The average installed capacities per technology as a share of the maximum allowed capacity for all nodes within each quadrant. The quadrants are defined based on whether the annual net demand is positive or negative in a node, as well as the production conditions for each technology in terms of FLH. As the number of nodes varies between quadrants, a change in one quadrant does not equal the same change in another quadrant in absolute capacity numbers. Results are shown for offshore wind, onshore wind, and solar PV, across both grid capacity levels.

of weather year can significantly influence the optimal generation mix, indicating the sensitivity of the results to weather variability.

In addition, the representation of hydropower, which is the predominant electricity generation technology in the region, is likely to influence the estimated need for peaking capacity. Previous studies (e.g., Fälth et al. [67] and Hirth [68]) have highlighted that aggregated representations of hydropower with perfect foresight in energy systems modeling, as is also the case in this study, tend to overestimate the flexibility provided by hydropower. A more-accurate approach to accounting for the physical constraints of rivers and reservoirs, as demonstrated by [69], involves the development of equivalent models that reduce storage and production capacities. The absence of such constraints in the present study may result in an underestimation of the required capacities for peaking technologies, such as gas turbines.

As a result of the aforementioned uncertainties, the absolute values related to flexibility measures, such as gas turbines and batteries, should be interpreted as indicative estimates rather than precise capacity requirements. Further model development and sensitivity analyses are needed to support more-robust conclusions regarding the optimal siting and scale of these technologies.

The sensitivity analysis conducted in this study indicates that while key assumptions do not significantly alter the overall system production mix, they can heavily influence the spatial distributions of wind and solar power generation. Specifically, the analysis reveals that up to 26% of renewable power production units would be relocated if the maximum theoretical thermal capacity of the grid was to be fully utilized. This effect is particularly pronounced for offshore wind, given its reliance on a limited number of sites with high potential annual production levels.

However, due to *n-1* security constraints, the assumption of full utilization of thermal capacity at all times is not realistic. A more-refined approach to representing grid capacity over time would entail incorporating weather-dependent transmission capacities, wherein transmission limits adjust dynamically based on the ambient temperature and wind speeds. Integrating such an approach represents a logical next step towards improving the applied modeling framework.

5. Conclusions

The number of FLH annually and proximity to net demand are critical factors influencing the siting of VRE technologies in the model.
 In general, onshore wind, offshore wind, and solar PV tend to be installed in nodes with high annual net electricity demands and favorable FLH potentials. However, each technology follows certain distinct trends:

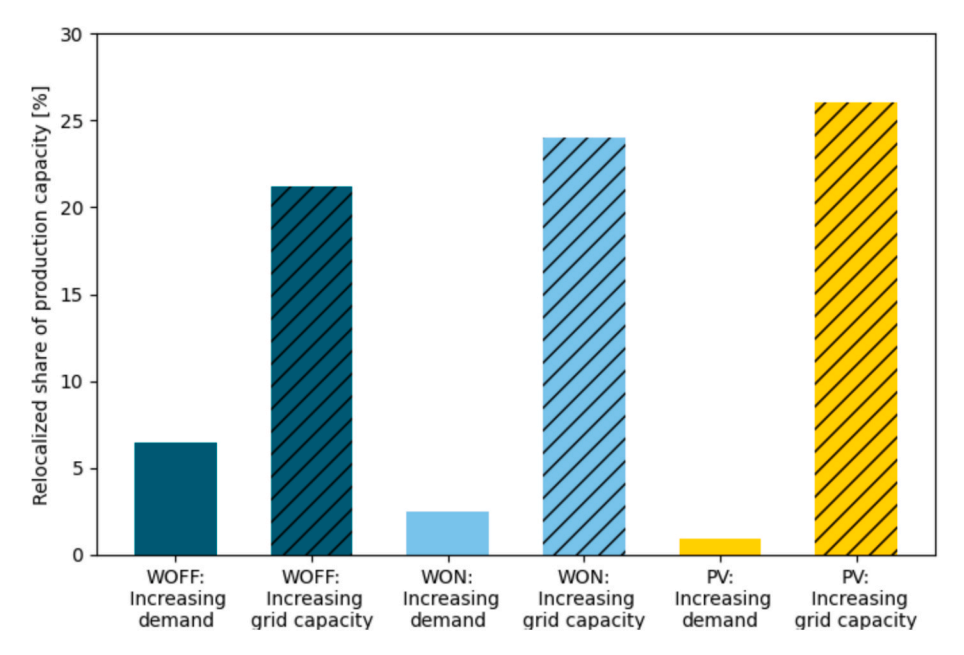


Fig. 15. The shares of production capacity that are relocated for two different changes in modeling inputs: (1) increasing the demand level from Moderate to High; and (2) increasing the grid capacity from Standard to High (in the High demand scenario). WOFF, offshore wind; WON, onshore wind; PV, photovoltaic.

Table 5Total system costs for the different modeling cases included in the sensitivity analysis. These costs encompass both investment and operational expenditures, as defined in Equation (1). The table also shows the proportion of total costs accounted for by investments.

Modeling case	Total system cost [GEUR]	Investment cost as share of total cost
Moderate demand, Grid factor 0.7	6.2	88 %
Moderate demand, Grid factor 1	5.3	86 %
High demand, Grid factor 0.7	12.6	86 %
High demand, Grid factor	11.1	85 %

- o Onshore wind prioritizes sites with the most-favorable wind conditions in the *Moderate demand scenario*. As the demand for electricity increases, the placement of additional capacity shifts toward locations that lie closer to major load centers, demonstrating high versatility in optimal siting decisions.
- o Optimal siting of offshore wind is primarily dictated by high numbers of FLH, regardless of the electricity demand levels. Its high capital costs require a high capacity factor to ensure cost efficiency.
- o Siting of solar PV shows the strongest correlation with positive annual net demand for electricity. Its strong variations in production amplitude make it less-suitable for long-distance transmission in a constrained grid, reinforcing a preference for local placement close to demand centers.
- Deviations from the expected correlation between FLH and net demand were identified:
 - o Colocation of both solar and wind power with existing nuclear production nodes occurs despite a negative net demand locally. These nodes benefit from a strong transmission infrastructure and are often situated in regions with electricity surpluses.
 - o Nodes in regions close to major demand centers attract investments in onshore wind and, to a lesser extent, solar PV, even at locations with low annual FLH potential.

- The optimal placement of gas turbines and batteries is strongly influenced by local grid conditions, demand center locations, and hydropower availability. In nodes where import capacity is limited relative to local demand, these technologies are deployed as a means to meet the nodal peak electricity demand. In addition, gas turbines and batteries are introduced to serve other functions, addressing regional power deficits and balancing solar power fluctuations, particularly in areas that lack hydropower resources.
- The sensitivity analysis underscores the significant impacts of grid capacity assumptions on the spatial distribution of renewable energy production. When 100% of the thermal grid capacity is utilized instead of 70%, 22%–26% of wind and solar power production is relocated. In contrast, variations in demand levels do not result in similarly pronounced shifts in the location of production units. This suggests that, provided that the geographic positioning of the future demand is known, uncertainties regarding its absolute magnitude are less-critical for determining the optimal siting of distributed generation technologies.

CRediT authorship contribution statement

Joel Bertilsson: Writing – original draft, Visualization, Methodology, Investigation, Formal analysis, Data curation, Conceptualization. **Lisa Göransson:** Writing – review & editing, Supervision, Methodology, Conceptualization. **Filip Johnsson:** Writing – review & editing, Supervision, Project administration, Funding acquisition, Conceptualization.

Funding

This study was supported financially by the Mistra Electrification program.

Declaration of competing interest

The authors declare that they have no known competing financial interests or personal relationships that could have appeared to influence the work reported in this paper.

Appendix A. Supplementary data

Supplementary data to this article can be found online at https://doi.org/10.1016/j.ref.2025.100765.

Data availability

Data and code will be made available publicly

References

- [1] International Energy Agency, "World Energy Outlook.," p. 39, 2024.
- [2] P.S. Georgilakis, N.D. Hatziargyriou, Optimal distributed generation placement in power distribution networks: Models, methods, and future research, IEEE Trans. Power Syst. 28 (3) (2013) 3420–3428, https://doi.org/10.1109/ TDWBS 2012 2237043
- [3] H.L. Willis, Analytical methods and rules of thumb for modeling DG-distribution interaction, Proc. IEEE Power Eng. Soc. Transm. Distrib. Conf. 3 (2000) 1643–1644, https://doi.org/10.1109/pess.2000.868774.
- [4] V.V.S.N. Murthy, A. Kumar, Comparison of optimal DG allocation methods in radial distribution systems based on sensitivity approaches, Int. J. Electr. Power Energy Syst. 53 (1) (2013) 450–467, https://doi.org/10.1016/j. iienes.2013.05.018.
- [5] R.K. Singh, S.K. Goswami, Optimum siting and sizing of distributed generations in radial and networked systems, Electr. Power Components Syst. 37 (2) (2009) 127–145, https://doi.org/10.1080/15325000802388633.
- [6] N. Rugthaichareoncheep, T. Lantharthong, A. Ratreepruk, J. Ratchatha, Application of Tabu search for optimal placement and sizing of distributed generation for loss reduction, Adv. Mater. Res. 433–440 (2012) 7190–7194, https://doi.org/10.4028/www.scientific.net/AMR.433-440.7190.
- [7] K. Mahesh, P. Nallagownden, I. Elamvazuthi, Optimal placement and sizing of distributed generators for voltage-dependent load model in radial distribution system, Renew. Energy Focus 19–20 (June) (2017) 23–37, https://doi.org/ 10.1016/j.ref.2017.05.003.
- [8] M. Kefayat, A. Lashkar Ara, S.A. Nabavi Niaki, A hybrid of ant colony optimization and artificial bee colony algorithm for probabilistic optimal placement and sizing of distributed energy resources, Energy Convers. Manag. 92 (2015) 149–161, https://doi.org/10.1016/j.enconman.2014.12.037.
- [9] N.S. Rau, Y.H. Wan, Optimum Location of Resources in Distributed Planning, IEEE Trans. Power Syst. 9 (4) (1994) 2014–2020, https://doi.org/10.1109/59.331463.
- [10] S. Kaur, G. Kumbhar, J. Sharma, A MINLP technique for optimal placement of multiple DG units in distribution systems, Int. J. Electr. Power Energy Syst. 63 (2014) 609–617, https://doi.org/10.1016/j.ijepes.2014.06.023.
- [11] N. Khalesi, N. Rezaei, M.R. Haghifam, DG allocation with application of dynamic programming for loss reduction and reliability improvement, Int. J. Electr. Power Energy Syst. 33 (2) (2011) 288–295, https://doi.org/10.1016/j. ijepes.2010.08.024.
- [12] P. Prakash, D.K. Khatod, Optimal sizing and siting techniques for distributed generation in distribution systems: A review, Renew. Sustain. Energy Rev. 57 (2016) 111–130, https://doi.org/10.1016/j.rser.2015.12.099.
- [13] S.A. Memon, R.N. Patel, An overview of optimization techniques used for sizing of hybrid renewable energy systems, Renew. Energy Focus 39 (December) (2021) 1–26, https://doi.org/10.1016/j.ref.2021.07.007.
- [14] M. Pesaran H.A, P. D. Huy, and V. K. Ramachandaramurthy, "A review of the optimal allocation of distributed generation: Objectives, constraints, methods, and algorithms," Renew. Sustain. Energy Rev., vol. 75, no. September 2015, pp. 293–312, 2017, doi: 10.1016/j.rser.2016.10.071.
- [15] T. Brown, D. Schlachtberger, A. Kies, S. Schramm, M. Greiner, Synergies of sector coupling and transmission reinforcement in a cost-optimised, highly renewable European energy system, Energy 160 (January) (2018) 720–739, https://doi.org/ 10.1016/j.energy.2018.06.222.
- [16] D.P. Schlachtberger, T. Brown, S. Schramm, M. Greiner, The benefits of cooperation in a highly renewable European electricity network, Energy 134 (2017) 469–481, https://doi.org/10.1016/j.energy.2017.06.004.
- [17] D.A. Copp, T.A. Nguyen, R.H. Byrne, B.R. Chalamala, Optimal sizing of distributed energy resources for planning 100% renewable electric power systems, Energy 239 (2022) 122436, https://doi.org/10.1016/j.energy.2021.122436.
- [18] D. Atsmon, L. Reichenberg, V. Verendel, MENA compared to Europe: The influence of land use, nuclear power, and transmission expansion on renewable electricity system costs, Energy Strateg. Rev. 33 (September) (2020) 2021, https://doi.org/ 10.1016/j.esr.2020.100590.
- [19] A. Aghahosseini, D. Bogdanov, and C. Breyer, "Towards sustainable development in the MENA region: Analysing the feasibility of a 100 % renewable electricity system in 2030," Energy Strateg. Rev., vol. 28, no. November 2018, p. 100466, 2020, doi: 10.1016/j.esr.2020.100466.
- [20] L. De Souza, N. Simas, D. Bogdanov, P. Vainikka, and C. Breyer, "Hydro, wind and solar power as a base for a 100 % renewable energy supply for South and Central America," PLoS One, pp. 1–15, 2017.
- [21] A. Aghahosseini, "A Techno-Economic Study of an Entirely Renewable Energy-Based Power Supply for North America for 2030 Conditions," Energies, vol. 10, no. 8, 2017, doi: 10.3390/en10081171.
- [22] M. Child, C. Kemfert, D. Bogdanov, C. Breyer, Flexible electricity generation, grid exchange and storage for the transition to a 100 % renewable energy system in

- Europe, Renew. Energy 139 (2019) 80–101, https://doi.org/10.1016/j.renene 2019 02 077
- [23] J. Gawlick, T. Hamacher, Impact of coupling the electricity and hydrogen sector in a zero-emission European energy system in 2050, Energy Policy vol. 180, no. June (2023) 113646, https://doi.org/10.1016/j.enpol.2023.113646.
- [24] H. Bjørnebye, C. Hagem, A. Lind, Optimal location of renewable power *, Energy 147 (714) (2018) 1203–1215, https://doi.org/10.1016/j.energy.2018.01.058.
- [25] M.M. Frysztacki, J. Hörsch, V. Hagenmeyer, T. Brown, The strong effect of network resolution on electricity system models with high shares of wind and solar, Appl. Energy 291 (October) (2020) 2021, https://doi.org/10.1016/j. appergy 2021 116726
- [26] M.M. Frysztacki, G. Recht, T. Brown, A comparison of clustering methods for the spatial reduction of renewable electricity optimisation models of Europe, Energy Informatics 5 (1) (2022) 1–27, https://doi.org/10.1186/s42162-022-00187-7.
- [27] V. Krishnan, W. Cole, Evaluating the value of high spatial resolution in national capacity expansion models using ReEDS, IEEE Power Energy Soc. Gen. Meet. vol. 2016-Novem (2016) 1–5, https://doi.org/10.1109/PESGM.2016.7741996.
- [28] K. Siala, M.Y. Mahfouz, Impact of the choice of regions on energy system models, Energy Strateg. Rev. 25 (June) (2019) 75–85, https://doi.org/10.1016/j. esr.2019.100362.
- [29] K. Phillips, J.A. Moncada, H. Ergun, "Spatial Clustering of Renewable Timeseries for Region Generation" (2022).
- [30] B.A. Frew, M.Z. Jacobson, Temporal and spatial tradeoffs in power system modeling with assumptions about storage: An application of the POWER model, Energy 117 (2016) 198–213, https://doi.org/10.1016/j.energy.2016.10.074.
- [31] C.E. Fleischer, "Minimising the effects of spatial scale reduction on power system models," Energy, Strateg. Rev. vol. 32, no. September (2020) 100563, https://doi. org/10.1016/j.esr.2020.100563.
- [32] M. Fürsch, S. Hagspiel, C. Jägemann, S. Nagl, D. Lindenberger, E. Tröster, The role of grid extensions in a cost-efficient transformation of the European electricity system until 2050, Appl. Energy 104 (2013) 642–652, https://doi.org/10.1016/j. apenergy.2012.11.050.
- [33] T. Tro, J. Lilliestam, S. Marelli, T. Tro, Article Trade-Offs between Geographic Scale, Cost, and Infrastructure Requirements for Fully Renewable Electricity in Europe Trade-Offs between Geographic Scale, Cost, and Infrastructure Requirements for Fully Renewable Electricity in Europe, Joule 4 (9) (2020) 1929–1948, https://doi.org/10.1016/j.joule.2020.07.018.
- [34] F. Obermüller, "Build wind capacities at windy locations? Assessment of system optimal wind locations," 2017.
- [35] ENTSO-E, "ENTSO-E Transmission System Map", [Online]. Available: https://www.entsoe.eu/data/map/.
- [36] Svenska Kraftnät, "Grid development plan," 2024. [Online]. Available: www.svk. se/siteassets/om-oss/rapporter/2024/grid development plan 2024-2033.pdf.
- [37] Nordic TSOs, "Nordic Grid Development Perspective 2023," Nord. Grid Dev. Perspect. 2023, 2023, [Online]. Available: https://www.statnett.no/globalassets/for-aktorer-i-kraftsystemet/planer-og-analyser/ngpd2023.pdf.
- [38] B. Stott, J. Jardim, O. Alsac, DC power flow revisited, IEEE Trans. Power Syst. 24 (3) (2009) 1290–1300, https://doi.org/10.1109/TPWRS.2009.2021235.
- [39] S. Frank, S. Rebennack, "An introduction to optimal power flow: Theory, formulation, and examples," IIE Trans. (Institute, Ind. Eng. 48 (12) (2016) 1172–1197, https://doi.org/10.1080/0740817X.2016.1189626.
- [40] O. Hodel, Henrik; Chen, Peiyuan; Göransson, Lisa; Carlson, "Modelling and validation of the Nordic transmission system based on open data," IET Conf. Proc., no. 16, 2024, [Online]. Available: https://doi.org/10.1049/icp.2024.377.
- [41] S.M. Fatemi, S. Abedi, S. Member, G.B. Gharehpetian, S.H. Hosseinian, M. Abedi, Introducing a Novel DC Power Flow Method With Reactive Power Considerations, IEEE Trans. Power Syst. 30 (6) (2015) 3012–3023, https://doi.org/10.1109/ TPWRS.2014.2368572.
- [42] Siemens., "HVDC Classic powerful and economical: High-performance power transmission," 2017. [Online]. Available: https://tinyurl.com/yy3ouxwm.
- [43] Iea, "Electricity Transmission and Distribution -, Technology Brief E12" (2014).
- [44] L. Göransson, J. Goop, M. Odenberger, F. Johnsson, Impact of thermal plant cycling on the cost-optimal composition of a regional electricity generation system, Appl. Energy 197 (2017) 230–240, https://doi.org/10.1016/j. apenergy.2017.04.018.
- [45] S. Oberg, M. Odenberger, and F. Johnsson, "The cost dynamics of hydrogen supply in future energy systems – A techno-economic study," Appl. Energy, vol. 328, no. October, 2022, doi: 10.1016/j.apenergy.2022.120233.
- [46] Danish Energy Agency, "Technology Data," 2023. https://ens.dk/en/our-services/ projections-and-models/technology-data.
- [47] Finansdepartementet, "Promemoria Finansiering och riskdelning vid investeringar i ny kärnkraft," p. 297, 2024, [Online]. Available: https://www.regeringen.se/ rattsliga-dokument/departementsserien-och-promemorior/2024/08/finansieringoch-riskdelning-vid-investeringar-i-ny-karnkraft/.
- [48] D.D. Papadias, R.K. Ahluwalia, Bulk storage of hydrogen, Int. J. Hydrogen Energy 46 (70) (2021) 34527–34541, https://doi.org/10.1016/j.ijhydene.2021.08.028.
- [49] N. Mattsson, V. Verendel, F. Hedenus, L. Reichenberg, An autopilot for energy models – Automatic generation of renewable supply curves, hourly capacity factors and hourly synthetic electricity demand for arbitrary world regions, Energy Strateg. Rev. 33 (2021) 100606, https://doi.org/10.1016/j.esr.2020.100606.
- [50] F. Hedenus, N. Jakobsson, L. Reichenberg, N. Mattsson, Historical wind deployment and implications for energy system models, Renew. Sustain. Energy Rev. vol. 168, no. June (2022) 112813, https://doi.org/10.1016/j. rser.2022.112813.

- [51] European Commission's Joint Research Centre, "JRC Hydro-power plants database", [Online]. Available: https://github.com/energy-modelling-toolkit/ hydro-power-database.
- [52] S. Bergström, "The HBV model. In: Singh VP (ed) Computer Models of Watershed Hydrology," Water Resour. Publ., pp. 443–476, 1995.
- [53] R. et al. . Scharff, Klimatförändringarnas inverkan på vattenkraftens produktionsoch reglerförmåga. 2023. [Online]. Available: https://energiforsk.se/media/ 32165/2023-924-klimatfo-ra-ndringarnas-inverkan-pa-vattenkraftensproduktions-och-reglerfo-rma-ga.pdf.
- [54] F. Larsson, Anton; Gunnarsson, Ingemar; Tengberg, [Online]. Available: https://www.goteborgenergi.se/Files/Webb20/Kategoriserad information/Forskningsprojekt/The GoBiGas Project Demonstration of the Production of Biomethane from Biomass v 230507_6_0.pdf?TS=636807191662780982, "The GoBiGas Project" (2023).
- [55] ENTSO-E, "ENTSO-E Transparency Platform." https://transparency.entsoe.eu/ (accessed Feb. 06, 2024).
- [56] M. Taljegard, L. Göransson, M. Odenberger, and F. Johnsson, "To represent electric vehicles in electricity systems modelling—aggregated vehicle representation vs. Individual driving profiles," Energies, vol. 14, no. 3, 2021, doi: 10.3390/ en140.30530
- [57] NordEnergi, "Study on opportunities and barriers to electrification in the Nordic region," p. 66, 2021, [Online]. Available: https://www.energiforetagen.se/ globalassets/dokument/nordenergi/electrification-in-the-nordics—nordenergi_19_ 05_2021.pdf.
- [58] Svenska kraftnät, "Långsiktig marknadsanalys Scenarier för kraftsystemets utveckling fram till 2050," 2024. [Online]. Available: www.svk.se.
- [59] Hydrogen Cluster Finland, "Clean hydrogen economy strategy for Finland," no. June, 2023, [Online]. Available: https://h2cluster.fi/industry-led-hydrogeneconomy-strategy-for-finland-published/.

- [60] M. Johnsson, Filip; Unger, Thomas; Löfblad, Ebba Hagberg, "Delrapport B2. Elektrifieringens betydelse för omställningen," 2022.
- [61] IEA, "Hydrogen production projects interactive map." https://www.iea.org/data-and-statistics/data-tools/hydrogen-production-projects-interactive-map (accessed Apr. 04, 2024).
- [62] Quantified Carbon, "Kraftsamling Elförsörjning Scanarioanalys 2050," pp. 1–115, 2022, [Online]. Available: https://www.svensktnaringsliv.se/bilder_och_dokument/is7vro_scenarioanalys290twhpdf_1187594.html/Scenarioanalys% 252B290%252BTWh.pdf.
- [63] Energiforsk, "Efterfrågan på fossilfri el Analys av högnivåscenario," 2021.
- [64] C. Lohr, et al., Spatial concentration of renewables in energy system optimization models, Renew. Energy 198 (April) (2022) 144–154, https://doi.org/10.1016/j. renene.2022.07.144.
- [65] M. Zeyringer, J. Price, B. Fais, P.H. Li, E. Sharp, Designing low-carbon power systems for Great Britain in 2050 that are robust to the spatiotemporal and interannual variability of weather, Nat. Energy 3 (5) (2018) 395–403, https://doi.org/ 10.1038/s41560-018-0128-x.
- [66] H. C. Bloomfield, D. J. Brayshaw, L. C. Shaffrey, P. J. Coker, and H. E. Thornton, "Quantifying the increasing sensitivity of power systems to climate variability," Environ. Res. Lett., vol. 11, no. 12, 2016, doi: 10.1088/1748-9326/11/12/124025.
- [67] H. Ek Fälth, N. Mattsson, L. Reichenberg, F. Hedenus, Trade-offs between aggregated and turbine-level representations of hydropower in optimization models, Renew. Sustain. Energy Rev. vol. 183, no. May (2023) 113406, https://doi.org/10.1016/j.rser.2023.113406.
- [68] L. Hirth, The benefits of flexibility: The value of wind energy with hydropower, Appl. Energy 181 (2016) 210–223, https://doi.org/10.1016/j. apenergy.2016.07.039.
- [69] D. Risberg, L. Soder, "Hydro power equivalents of complex river systems," 2017 IEEE Manchester PowerTech, Powertech 2017 (2017), https://doi.org/10.1109/ PTC.2017.7981057.